

## Determining the physical conditions of extremely young Class 0 circumbinary disk around VLA1623A

CHENG-HAN HSIEH,<sup>1,2</sup> SHIH-PING LAI,<sup>1,3,4</sup> POU-IENG CHEONG,<sup>3</sup> CHIA-LIN KO,<sup>3,5</sup> ZHI-YUN LI,<sup>6</sup> AND NADIA M. MURILLO<sup>7</sup>

<sup>1</sup>*Department of Physics, National Tsing Hua University, 101 Section 2 Kuang Fu Road, 30013 Hsinchu, Taiwan*

<sup>2</sup>*Department of Astronomy, Yale University, New Haven, CT 06511, USA*

<sup>3</sup>*Institute for Astronomy, National Tsing Hua University, 101 Section 2 Kuang Fu Road, 30013 Hsinchu, Taiwan*

<sup>4</sup>*Academia Sinica Institute of Astronomy and Astrophysics, PO Box 23-141, 10617 Taipei, Taiwan*

<sup>5</sup>*Department of Physics, National Taiwan Normal University, No.162, Sec.1, Heping East Road, Taipei 10610, Taiwan*

<sup>6</sup>*Department of Astronomy, University of Virginia, 530 McCormick Road Charlottesville VA, USA*

<sup>7</sup>*Leiden Observatory, Leiden University, PO Box 9513, 2300 RA Leiden, The Netherlands*

(Received January 1, 2019)

Submitted to ApJ

### ABSTRACT

Observation and detailed modeling are carried out to probe the physical conditions of a Class 0 Keplerian circumbinary disk, VLA1623A. From the Atacama Large Millimeter/sub-millimeter Array (ALMA) Cycle 2 C<sup>18</sup>O J = 2-1 data, we found a rich extended structure in Position-Velocity (PV) diagram that cannot be fitted with a simple flat disk model. Large scale structures and accretion flows are identified by dendrogram analysis. 3D flared disk models are compared with observational data using PV diagrams. We model the motion of the circumbinary disk with flat and flared radiative transfer models and constrain the disk radius to be 180 AU with a vertical scale height less than 15 AU at 100 AU. Perhaps most interestingly, the kinematics of the gas traced by C<sup>18</sup>O deviate significantly on the 60AU-scale of the circumbinary disk around the protobinary VLA1623A, possibly indicating gas flowing across a gap from the circumbinary disk onto the central binary. Higher resolution observations are needed to test this interpretation.

*Keywords:* star formation – individual objects: VLA1623 – accretion disks – methods: observational  
– stars: low-mass – techniques: interferometric

### 1. INTRODUCTION

Around 50 percent of solar mass stars form in multiple systems (Raghavan et al. 2010). Multiplicity fraction increases for higher mass stars (Sana, & Evans 2011). These multiple systems are formed in the early stage of star formation via three processes: turbulent fragmentation, thermal fragmentation of rotating cores, and disk fragmentation. Turbulent and thermal fragmentation occurs relatively large scales, forming wide binaries with separation of order 1000 AU or larger. (Padoan, & Nordlund 2002; Offner et al. 2010; Inutsuka, & Miyama 1992; Burkert, & Bodenheimer 1993; Boss, & Keiser 2014; Pineda et al. 2015). As for the disk fragmentation, it is believed to be one of the primary processes

for forming close ( $\sim 100$  AU) binaries (Takakuwa et al. 2012; Tobin et al. 2013).

Previous observations have found many circumbinary disks (Takakuwa et al. 2012; Tobin et al. 2013; Dutrey et al. 2014, 2016; Chou et al. 2014; Tang et al. 2014, 2016). Near-infrared surveys of Class I sources have found that around 15 out of 88 targets have binary separations between 50 to 200 AU (Connelley et al. 2008; Duchêne et al. 2007). Despite the current progress, the multiplicity for Class 0 sources is still poorly understood due to its deeply embedded nature. Since disk fragmentation requires massive gravitationally unstable disks, close binary and multiplicity systems are expected to form in the early phase of star formation. Thus understanding the gas dynamics in extremely young Class 0 protobinary disk is crucial for testing binary formation theory.

Not only close multiplicity studies for Class 0 disk are limited, the mechanism for forming Class 0 disks is still

under debate. Numerical models simulating the collapse of a magnetized envelope with the assumption of ideal magnetohydrodynamics (MHD) show that disk formation is hindered by magnetic braking effects (Mellon, & Li 2008). One solution proposed is that magnetic braking efficiency can be reduced if the rotation axis is misaligned with the magnetic field direction (Hennebelle, & Ciardi 2009). Moreover, non-ideal MHD effects on disk formation have also been explored. Recently, 3D non-ideal MHD simulations have been carried out and a disk around 5 AU is formed at the end of the first core phase (Tomida et al. 2015).

A fundamental question that has yet to be answered is how does Class 0 disks grow in size and possibly fragment? A well-studied Class 0 candidate, HH212 is found to have a Keplerian disk within the 44 AU centrifugal barrier (Lee et al. 2017). The Keplerian disk of Class 0 protostar L1527 has a disk radius of 74 AU and the scale height at 100 AU is 48 AU (Aso et al. 2017; Tobin et al. 2013). As for VLA1623A, the Keplerian rotating disk size is fitted to 150 AU using  $C^{18}O$  as a tracer (Murillo et al. 2013). These observational results show Class 0 disks with varying disk sizes and structures.

The question of why these Class 0 disks have different structures, sizes and how they fragment has not been fully addressed. The discovery of extremely large ( $> 70AU$ ) Class 0 rotationally supported disks, L1527 (Aso et al. 2017; Tobin et al. 2013) and VLA1623A (Murillo et al. 2013), provide possible candidates to study disk fragmentation around Class 0 sources. Not much is known about how large rotationally supported disks are formed, and what factors influence their formation. In the recent analytical study carried out by Hennebelle et al. (2016), a relationship between disk radius and magnetic fields in the inner part of the core is found. The weak dependence of various relevant quantities suggests that Class 0 disks have a typical disk size  $\sim 18 AU$  (Hennebelle et al. 2016).

VLA1623-2417 (VLA1623 hereafter) is a triple non-coeval protostellar system, located at  $120 \pm 4.5 pc$  away in cloud  $\rho$  Ophiuchus A (Andre et al. 1993; Loinard et al. 2008; Ortiz-León et al. 2017)<sup>1</sup>. The system consists of three components: VLA1623A (Class 0 source), VLA1623B (younger than VLA1623A, possibly a transition between starless core and Class 0) (Santangelo et al. 2015), and VLA1623W (Class 1) (Murillo, & Lai 2013). Recent high angular resolution ( $\sim 0''.16$ ) 0.88 mm con-

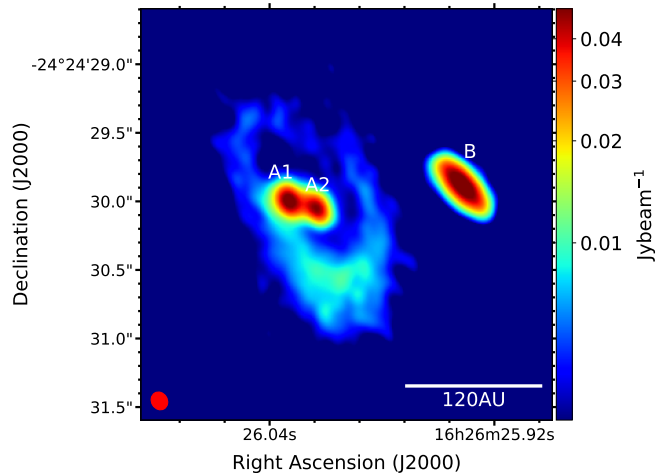


**Figure 1.** VLA1623 0.88 mm continuum image. The Class 0 source, VLA1623A is resolved into 2 sources, VLA1623A1 and VLA1623A2. The red ellipse marks the beam size.

tinuum data reveals that VLA1623A is in fact a binary denoted as VLA1623A1 and VLA1623A2 in Figure 1, and the Keplerian disk previously discovered is a circumbinary disk (Harris et al. 2018). The plane of sky separation between the VLA1623A1 and VLA1623A2<sup>2</sup> is around  $0''.2$ , which corresponds to a physical scale of 24 AU. Unfortunately, our Cycle 2  $C^{18}O$  ( $J = 2-1$ ) data with beam size  $0''.5$  cannot resolve the two sources ( $C^{18}O$  Moment maps shown in Figure 2).

With the increase of antennas and the UV-coverage, Cycle 2 data picks up significantly more  $C^{18}O$  emission than Cycle 0 observations shown in Figure 3. VLA1623A, being one of the youngest protobinary disks ever discovered is thus the perfect candidate to study disk fragmentation around Class 0 sources. In this project we aimed to trace mass accretion streams feeding the circumbinary disk all the way down to the central binary.

In what follows, in Section 2 we discuss the data used in this analysis. In Section 3 we compare Cycle 0 and Cycle 2  $C^{18}O$  data and highlight major emission components that would be further explored. In Section 4 we present our main results of foreground fitting, dendrogram analysis (Cheong et al. in prep.), flat and flared disk modeling, and accretion shocks analysis. In Section 5, we summarized the physical conditions of the VLA1623A circumbinary disk and its surrounding environment. In Section 6, we give our conclusions.

<sup>2</sup> The nomenclature used in Harris+2018 is VLA1623Aa and VLA1623Ab. However, the lower case letters after a source name are reserved for planets. IAU stipulated convention for stars should be VLA1623A1 and VLA1623A2.

<sup>1</sup> In this paper, the distance of 120 pc (Murillo, & Lai 2013) is used in the modelling instead of 137.3 pc (Ortiz-León et al. 2017). The physical scale would increase by a factor of 1.14 if the 137.3 pc distance is adopted.

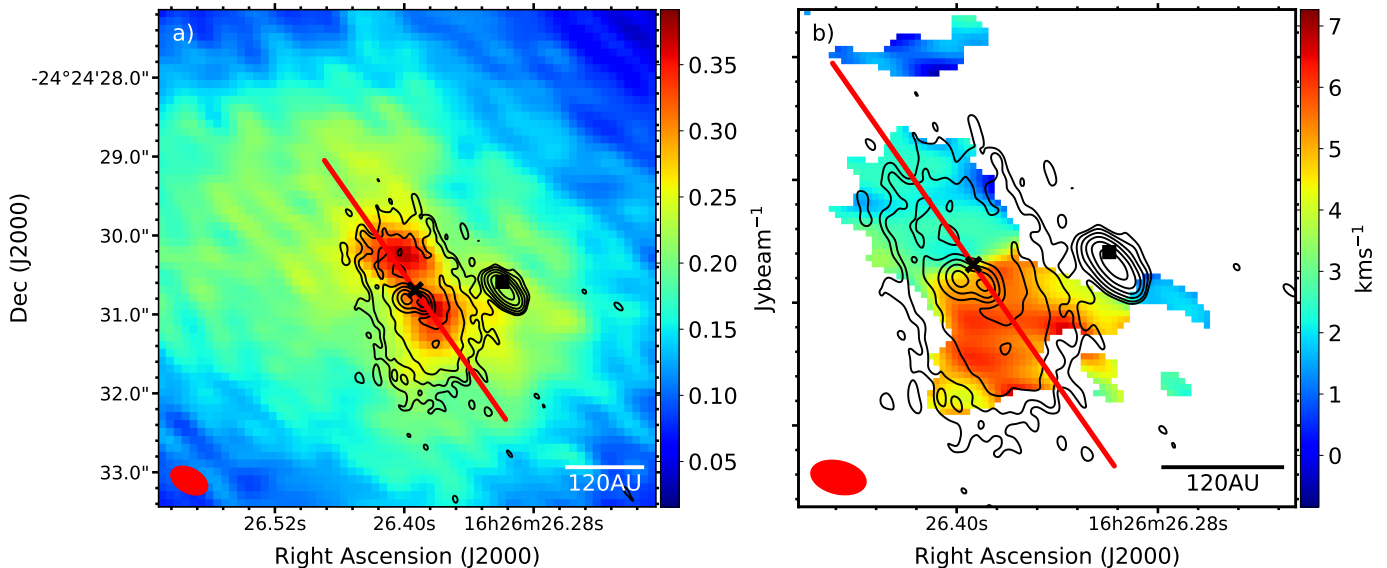


**Figure 2.** (a). VLA1623 0.88 mm continuum (contours) overlaid on the C<sup>18</sup>O integrated intensity map (color). VLA1623A and B's position are marked with a cross and a square, respectively. The color represents the C<sup>18</sup>O J = 2-1 integrated intensity map (moment 0) using combined data from ALMA 12m array and 7m array. The black contours are 0.88 mm continuum data in steps of  $3\sigma$ ,  $5\sigma$ ,  $10\sigma$ ,  $20\sigma$ ,  $40\sigma$ ,  $80\sigma$ , where  $\sigma = 5 \times 10^{-4}$  Jy beam<sup>-1</sup>. The red line indicates the location of the position velocity cut used in this study (PA = 209.82°, centered at VLA1623A). (b). VLA1623 0.88 mm continuum (contours) overlaid on the C<sup>18</sup>O intensity weighted velocity map (color).

**Table 1.** Summary of the observational data used in the analysis

Line	Transition	$\nu$ (GHz)	Beam Size ( $''$ )	Channel Widths (kms <sup>-1</sup> )	Rms noise (mJy beam <sup>-1</sup> )	PI
C <sup>18</sup> O	2-1	219.56036	$0''.52 \times 0''.31$	0.0832	9	
			$1''.10 \times 0''.89$	0.0208	18	Shih-Ping Lai
			$0''.51 \times 0''.31$	0.0208	14	
DCO+	3-2	216.11402	$0''.51 \times 0''.31$	0.085	5	Shih-Ping Lai
SO	$\nu = 0,$ $J = 8_8 - 7_7$	344.31061	$1''.11 \times 0''.76$	0.212	20	Victor Magalhães
Continuum	...	336.50000	$0''.13 \times 0''.12$	53309.11	0.5	Leslie Looney
Total Power Array	...	219.56036	$29''.67 \times 29''.67$	0.0208	500	Shih-Ping Lai

## 2. OBSERVATIONS

### 2.1. C<sup>18</sup>O

We observed VLA1623 with Atacama Large Millimeter/submillimeter Array (ALMA) in Cycle 2 with pointing coordinates ( $\alpha$ (J2000) = 16<sup>h</sup>26<sup>m</sup>26<sup>s</sup>.390,  $\delta$ (J2000) = -24°24'30".688) (project ID: 2013.1.01004S, PI: Shih-Ping Lai). The 12 m array configurations are C34-5 and C34-1. We also include the 7m Atacama Compact Array (ACA) (hereafter 7m array) and Total Power Array of ACA in our analysis. The 12m array data and 7m array data are combined via the CASA task CLEAN with a weighting parameter of Briggs -1.5, Briggs -1.0, and a natural weighting. These maps are used for identifying accretion flows, comparing with ALMA C<sup>18</sup>O Cycle 0 data, and analysis of disk motion respectively.

For the Briggs -1.5 weighting, the UV taper range is  $0''.25$ . The resulting C<sup>18</sup>O (J = 2-1) channel map has a resolution of  $1''.1 \times 0''.89$  (P.A. = 36.8°) with rms noise level at 18 mJy beam<sup>-1</sup>. The velocity resolution is 0.0208 km s<sup>-1</sup> with rest frequency at 219.56036 GHz (corresponding to a system velocity of 4.0 km s<sup>-1</sup> away in the line of sight). The low resolution data is used for dendrogram analysis and for identifying large structures around the circumbinary disk VLA1623.

For the natural weighted data, Hogbom algorithm is used for the deconvolution process resulting the resolution of  $0''.52 \times 0''.31$  (P.A. = 87.89°) with rms noise level at 9 mJy beam<sup>-1</sup>. The velocity resolution of 0.0832 km s<sup>-1</sup> is used to achieve a higher signal to noise ratio for disk modeling.

For comparison purposes, Briggs -1.0 weighting with UV taper range  $0''.25$  is applied to the Cycle 2  $C^{18}O$  data to achieve resolution  $0''.51 \times 0''.31$  (P.A. =  $61.83^\circ$ ) with rms noise level at  $14 \text{ mJy beam}^{-1}$ . The velocity resolution is  $0.0208 \text{ km s}^{-1}$ . This data set is only used to compare with Cycle 0 observation in Figure 3.

The  $C^{18}O$  mean velocity map (Figure 2 b.) shows a rotating disk around VLA1623A. In this study, all the position-velocity (PV) diagrams will be cut along the red line in Figure 2. The combined natural weighted  $C^{18}O$  data for 12m array configuration C34-5 (baseline range  $18.9 \sim 1090 \text{ m}$ ), C34-1 (baseline range  $14.2 \sim 347.3 \text{ m}$ ), and 7m array (baseline range  $7.1 \sim 48.9 \text{ m}$ ) data will be used in the analysis.

As for the Total Power Array data, the angular resolution is  $29''.67 \times 29''.67$  (P.A. =  $0.0^\circ$ ) with rms noise level at  $0.5 \text{ Jy beam}^{-1}$ . The script provided by ALMA Regional Center (ARC) is used to calibrate and reduce the data. The Total Power Array data would be used for the foreground study of the VLA1623A circumbinary disk.

### 2.2. Continuum data

We use the high resolution continuum data from the ALMA Archive (project ID: 2015.1.00084S, PI: Leslie Looney) see Table 1. The observation is done in Band 7 with an integration time of 4798 seconds. The continuum data is prepared by using CASA task CLEAN with uniform weighting. The synthesized beam is  $0''.13 \times 0''.12$  (P.A. =  $31.00^\circ$ ) with rms noise level at  $0.5 \text{ mJy beam}^{-1}$ .

### 2.3. $DCO^+ J = 3 - 2$ data

The  $DCO^+$  data used in this paper are from ALMA Cycle 2 observation in Band 6 of the 12m array combined with the observation from the 7m array. The data is prepared by the CASA task CLEAN with a weighting parameter of robust -0.5, and the UV taper range is set to  $1''.0$ . The rms noise level of  $DCO^+$  data is  $5 \text{ mJy beam}^{-1}$  and the synthesis beam size is  $0''.51 \times 0''.31$  (P.A. =  $63.05^\circ$ ). The velocity resolution of  $DCO^+$  data is  $0.085 \text{ km s}^{-1}$ .

### 2.4. $SO (\nu = 0, J = 8_8 - 7_7)$ data

In this paper, we present the results of the newly released ALMA Cycle 4  $SO \nu = 0, J = 8_8 - 7_7$  archival data (project ID: 2016.1.01468S, PI: Victor Magalhaes) to trace accretion shocks (See Table 1). The observation is carried out by ALMA on March 4 in 2017 with a maximum UV baseline of  $\sim 250 \text{ m}$ . The data is calibrated by the ALMA calibration script, and the imaging is carried out via the CASA task CLEAN with a weighting parameter of robust 0.0. The resulting synthesized beam has

an angular resolution of  $1''.11 \times 0''.76$  (P.A. =  $82.59^\circ$ ) with rms noise level at  $20 \text{ mJy beam}^{-1}$ . The largest recoverable angular scale is around  $3''.5$ . The spectral resolution is  $0.212 \text{ km s}^{-1}$ , and the  $SO (\nu = 0, J = 8_8 - 7_7)$  data have a line width larger than  $8 \text{ km s}^{-1}$  resulting in a line width to channel width ratio  $\sim 37$ .

## 3. RESULTS

### 3.1. The comparison between Cycle 0 and Cycle 2 data

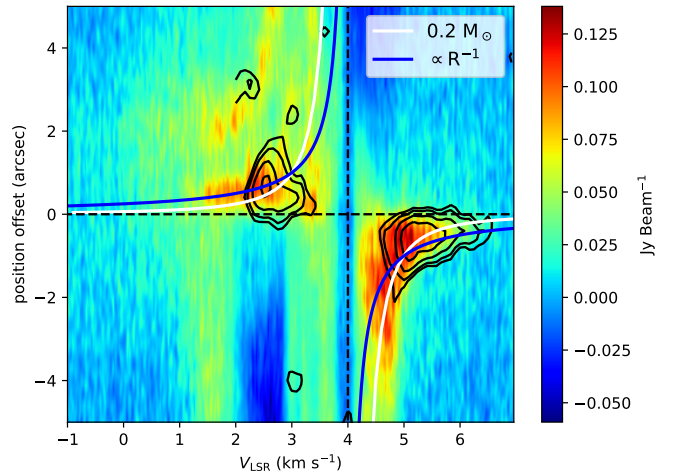


**Figure 3.** VLA1623A  $C^{18}O J = 2-1$  PV diagram. The black contours marked the ALMA Cycle 0  $C^{18}O J=2-1$  data, and the color background represents ALMA Cycle 2  $C^{18}O J=2-1$  data. The blue line represents the in-fall velocity profile with conserved specific angular momentum. The white line represents the Keplerian rotation profile with a central mass of  $0.2 M_\odot$ .

Figure 3 shows the comparison between the Cycle 0 (project ID: 2011.0.00902.S, PI: Nadia Murillo) and Cycle 2 (project ID: 2013.1.01004S, PI: Shih-Ping Lai) ALMA data. In the Cycle 2 data shown as color background, we identified a high-velocity blue-shifted emission around  $1.5 \text{ km s}^{-1}$ , and the red-shifted emission extends to  $4''.0$ . These features do not show in the Cycle 0 observations because there is not enough sampling in the short baselines.

Cycle 0 consists of only 16 antennae with a maximum baseline of  $\sim 400 \text{ m}$ . The beam-size is around  $0''.79 \times 0''.61$  with velocity resolution of  $0.0833 \text{ km s}^{-1}$  (Murillo et al. 2013). The largest recoverable angular scale is around  $2''.46$ . In comparison, Cycle 2 observations have increased sensitivity from the larger number of antennas and larger recoverable scale. More  $C^{18}O$  emission is recovered. Thus, the previous disk size and the structure of VLA1623A Keplerian disk needs to be reanalyzed.

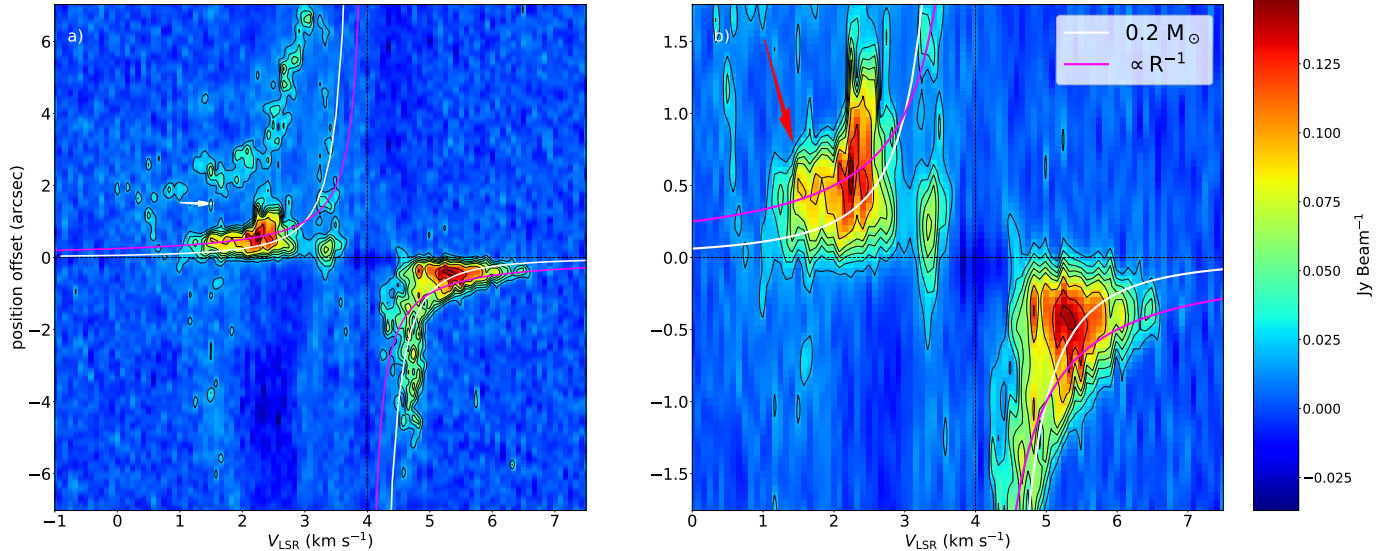


**Figure 4.** (a). Position-Velocity (PV) cut of  $C^{18}O$   $J = 2-1$  ALMA Cycle 2 VLA1623A Keplerian disk. Centered at VLA1623A with position angle  $209.82^\circ$  degrees. The magenta line represents the in-fall velocity profile with conserved specific angular momentum. The white line represents the Keplerian rotation profile with a central mass of  $0.2 M_\odot$ . The white arrow marks the position of a gap between accretion flow and the Keplerian disk. (b). The zoomed in image of (a). Note the red arrow highlights a super-Keplerian rotation region.

### 3.2. Position velocity diagram

To identify the gas kinematics, we create position-velocity (PV) diagrams centered at VLA1623A along the red line shown in Figure 2. Since the binary separation is within our beam-size, the results are the same when we shift the PV cut from one component to the other. Thus we select the center of  $C^{18}O$  emission for our PV diagrams. From the rotation curves, the Keplerian rotation with a central star mass  $0.2 M_\odot$  best fits the PV data. This is consistent with the results of Murillo using Cycle 0 data. Thus the combined mass for the VLA1623A1 and VLA1623A2 binary is constrained to be around  $0.2 M_\odot$ .

In the high-velocity blue-shifted part we observed a strong emission above the Keplerian rotation white line (marked by a red arrow in Figure 4). The emission between  $1.5 \text{ km s}^{-1}$  and  $2.0 \text{ km s}^{-1}$  is reasonably well fitted with the in-fall line (with conserved angular momentum). This feature has not been seen in the Cycle 0 observation.

## 4. ANALYSIS

Is this high-velocity blue-shifted component part of the Keplerian disk? Is it due to a flared Keplerian disk with projection effects? Or is it accretion flows or other large structures in the line of sight? To determine the nature of this super-Keplerian rotation component we will conduct an analysis to identify foregrounds, accretion flows, large scale structures, and the flared Keplerian disk.

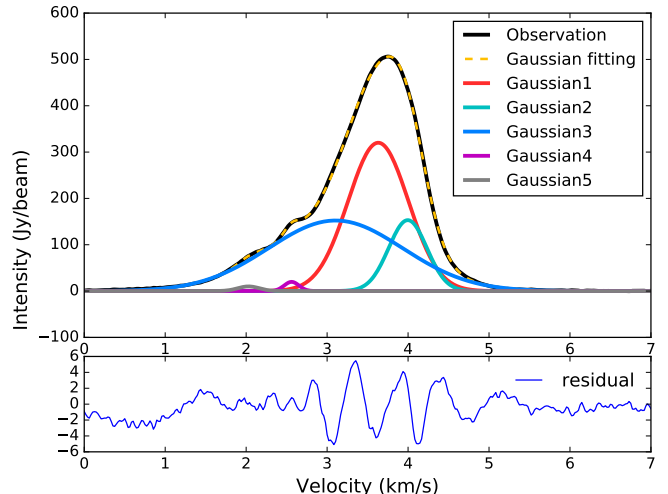


**Figure 5.** Gaussian fit of a total power spectrum of VLA1623. The black line represents the observational data for the Total Power Array, and the color lines represent the Gaussian fitting result.

### 4.1. Foreground study of VLA1623

The total power spectrum data is used to determine the strength and positions of the foregrounds of VLA1623. We did not combine the Total Power data with the 12m+7m array data in order to separate the compact disk emission from the large-scale cloud emission. In Figure 5, five Gaussian functions are used to fit the total power spectrum with the best fit result shown in Table 2. The maximum foreground component which corresponds to the envelope of the VLA1623

**Table 2.** Total Power Spectrum fitting results (Foreground components)

Number	Velocity (kms <sup>-1</sup> )	Amplitude (Jy)	Widths (kms <sup>-1</sup> )
1	3.632	320.19	0.2782
2	3.996	153.11	0.1117
3	3.104	152.29	1.3790
4	2.561	19.87	0.0164
5	2.029	10.04	0.0348
$\sigma = 0.353(Jy)$ $\chi^2 = 9401.49$ $\chi^2/dof = 29.29$			

system is located at a velocity of 3.632 km s<sup>-1</sup>. In Figure 3 at the system velocity 4.0 km s<sup>-1</sup> the C<sup>18</sup>O suffers a huge absorption and this is consistent with our Gaussian fitted foreground component 2 shown in Figure 5. As for other minor components located at velocities 3.104, 2.029, and 2.561 km s<sup>-1</sup>, their physical origins and whether or not they are part of the VLA1623 system are unclear. Furthermore, all the absorption foregrounds including the central envelope are located in the blue-shifted region which is consistent with the preliminary estimations done by Murillo et al. (2013).

The foreground absorption is not included in the flat and flared disk models (Section 4.3 and 4.4). Since the exact strength of the foreground components is uncertain, and the low spatial resolution of data would make any modeled foreground highly artificial and model dependent. The purpose of this foreground analysis is to identify the velocity of foreground components. When comparing the data with models, we will avoid these components.

#### 4.2. Using Dendrograms to identify Accretion flows and set constraint on disk size

A Class 0 protostar is actively accreting and is still deeply embedded in the envelope. With infalling streamers feeding material from the envelope onto the circumbinary disk and outflows, it is challenging to identify disks around Class 0 sources. In order to determine the disk size in a Class 0 source, we need to identify outflows, envelope, accretion flows and other large scale structures. Outflows have been observed in <sup>12</sup>CO by (Andre et al. 1990; Dent et al. 1995; Yu & Chernin 1997). As for the envelope, which is located at 3.6 km s<sup>-1</sup> fitted by the total power spectrum, can be separated out from the rest of the components in velocity domain.

In our study, the C<sup>18</sup>O traces both the rotational disk and accretion flows around it. Dendrogram algorithm is used to identify the connected structures in the Position-position-velocity (PPV) space (Cheong et al. in prep; see Figure 6). The algorithm identifies in total 7 ma-

ior branches (local maximum) labeled in Figure 6. In addition to the 6 major branches found in (Cheong et al. in prep), we found another large structure, blue-shifted III component, connected to the VLA1623A circumbinary disk. In the following sections, we use SO as a shock tracer to identify the interactions between accretion flows and the circumbinary disk (See Table 3, Figure 17).

Besides the blue-shifted III component, Cheong et al. (in prep.) further compared the data with the CMU model (Ulrich 1976; Cassen, & Moosman 1981), a rotating collapse model with conserved specific angular momentum, and found that the red-shifted VI component and blue-shifted I component are accretion flows connected to the central Keplerian disk (channel maps shown in Figure 7 & Figure 8).

Figure 7 shows the channel maps of the blue-shifted I component identified by the dendrogram. The 0.88 mm continuum data is shown as the magenta contours which mark the location of the VLA1623A circumbinary disk and VLA1623B. Inside the magenta contours, the C<sup>18</sup>O emission shows the blue-shifted I accretion flows are faintly connected to the central disk. The drop of C<sup>18</sup>O intensity between the disk and large structure I indicates a clear gap around 120 AU exists between the large scale structure and the Keplerian disk. The Keplerian disk is constrained to roughly 180 AU from the blue-shifted channel maps.

Figure 8 shows the channel maps of the red-shifted accretion flow VI connected to the central disk. In the velocity channels between 4.17 to 5.00 km s<sup>-1</sup>, the accretion flow is well mixed with the disk and the C<sup>18</sup>O emission extends to 6''0 (~ 500 AU). Only in the high-velocity channels (> 5.1 km s<sup>-1</sup>), the C<sup>18</sup>O emission traces the Keplerian disk without any contamination from the accretion flow. High-velocity channels are not contaminated by accretion flows, but they only provide the information in the inner region in the Keplerian disk. Thus the disk size can't be determined by the red-shifted channels.

From the rotation curves in Figure 4, we deduce the motion of the disk is Keplerian. And hence without loss of generality, we can assume the disk is axially symmetric and use the blue-shifted side to constrain the disk size. We select the continuum level such that the edge of the disk matches the boundary of the gap in Figure 7. Therefore, the circumbinary disk size is constrained to be 180 AU. Furthermore, the extended emission between 4 km s<sup>-1</sup> and 5 km s<sup>-1</sup> in Figure 3 is likely a mixture of accretion flow and disk components. We will explore this more in the following sections. More technical details of

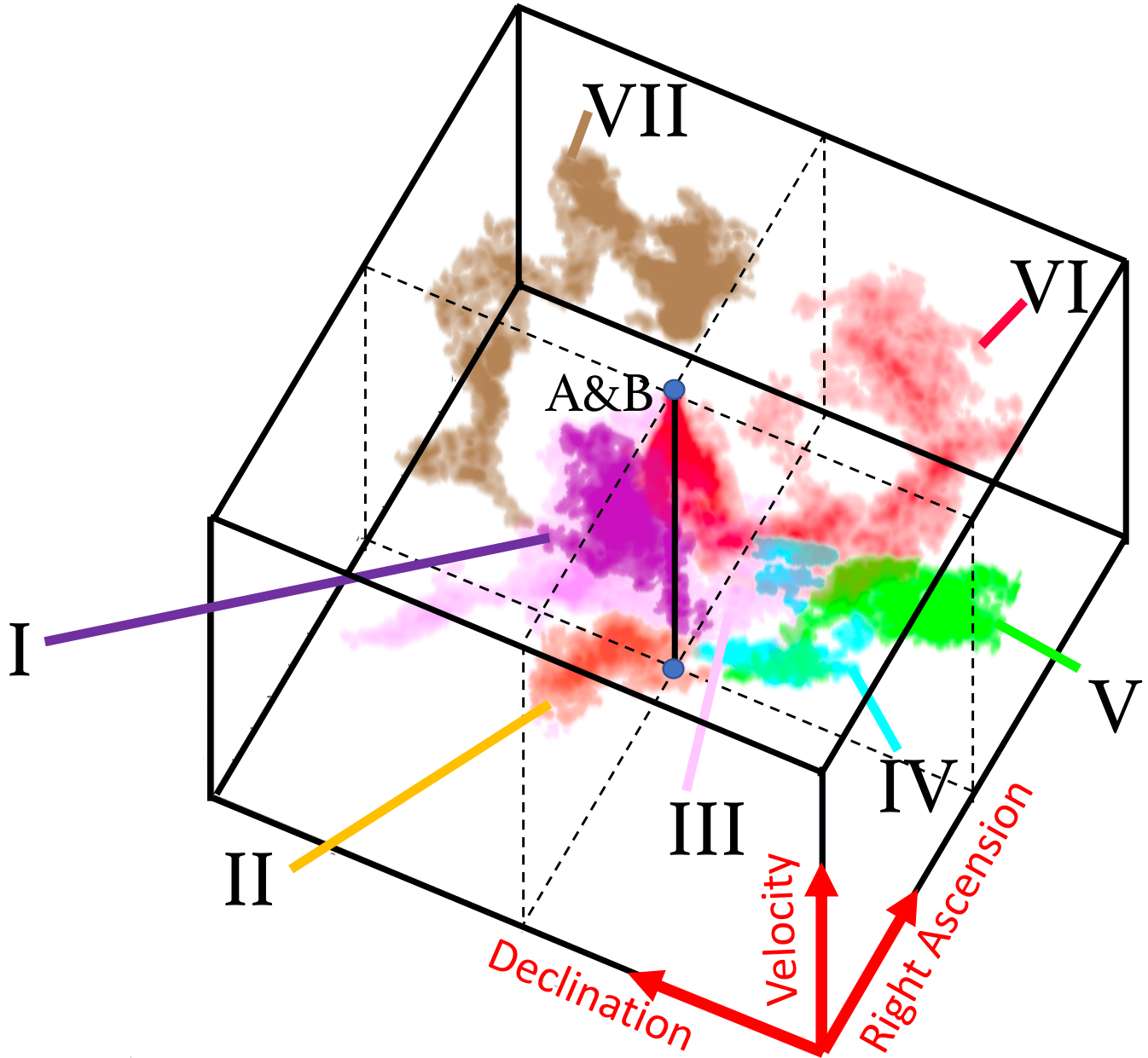


**Figure 6.** 3D Dendrogram around VLA1623 system. The  $\text{C}^{18}\text{O}$  large structures are labeled with Roman numerals. The central black line marked the position of VLA1623A and VLA1623B in the PPV cube. The 3D image is made by using GLUE visualization software (Beaumont et al. 2014). For the detailed analysis of dendrograms please see Cheong et al. (in prep.).

dendrogram data preparation and accretion flows modeling can be found in Cheong et al. (in prep.)’s paper.

#### 4.3. Flat Disk Model

We first model the ALMA Cycle 2  $\text{C}^{18}\text{O}$   $J = 2-1$  position-velocity (PV) diagram of the VLA1623A circumbinary disk with a Flat Keplerian disk model. The PV diagram are cut along the red line in Figure 2. The governing equations for the velocity, temperature, and column density profiles in the flat Keplerian disk are

described as the following:

$$v(R) = \sqrt{\frac{GM_*}{R}} \quad (1)$$

$$T(R) = T_0 \times \left(\frac{R}{100\text{AU}}\right)^{-0.5} \quad (2)$$

$$\Sigma(R) = \Sigma_0 \times \left(\frac{R}{100\text{AU}}\right)^{-1} \quad (3)$$

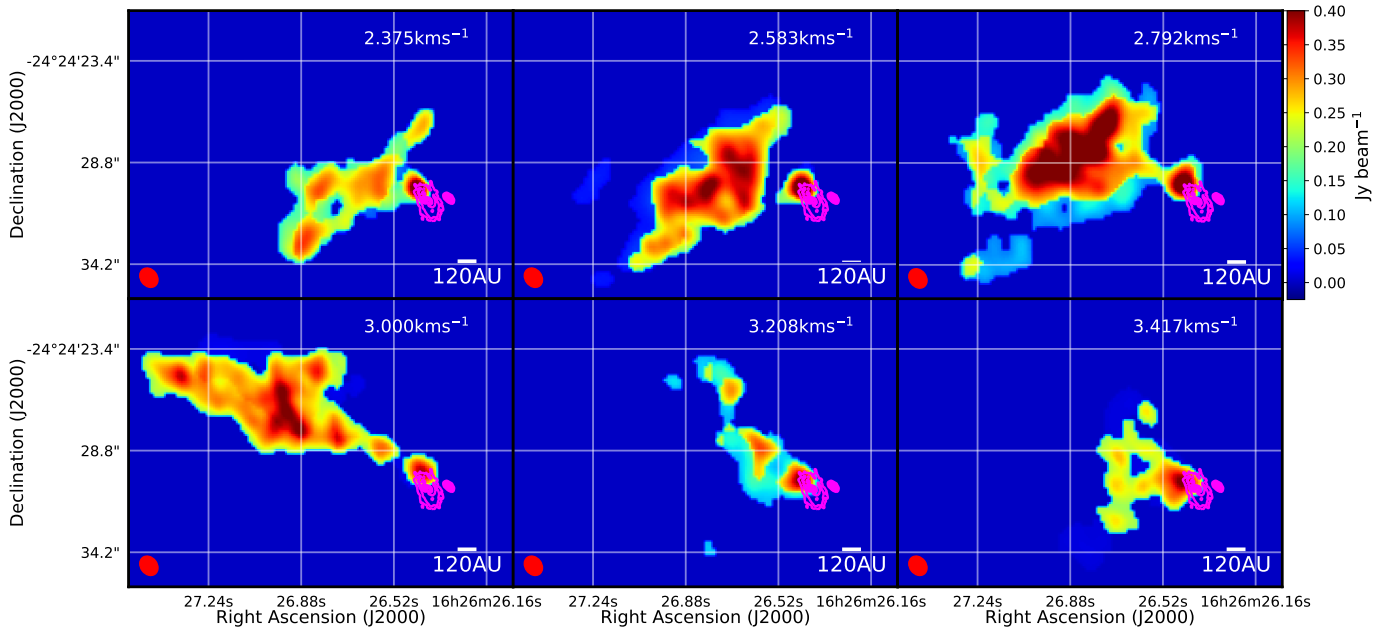


**Figure 7.** VLA1623A and blue-shifted accretion flow I channel maps. The color represents the  $C^{18}O$   $J = 2-1$  emission identified by the dendrogram algorithm. The dendrogram corresponds to the Purple component (accretion flows and disk) in Cheong et al. (in prep.)’s paper. The magenta contours are 0.88 mm continuum data. The contours are in steps of  $3\sigma$ ,  $5\sigma$ ,  $10\sigma$ ,  $20\sigma$ ,  $40\sigma$ ,  $80\sigma$ , where  $\sigma = 5 \times 10^{-4}$   $Jy\ beam^{-1}$ ).

For the column density at 100 AU ( $\Sigma_0$ ), we adopted the number to be  $6.173 \times 10^{21} \text{ cm}^{-2}$ , and the disk inclination angle is  $55^\circ$  (Murillo et al. 2013). For temperature distribution we assume the temperature power law exponent to be  $-0.5$ , and we adopted a temperature of  $\sim 30$  K at 100 AU based on the  $DCO^+$  5-4/3-2 data (Murillo et al. 2018).

A flat disk model is first generated using Equation 1, Equation 2, and Equation 3. Then the simulated disk is convolved with the ALMA telescope beam using CASA SimObserve and CASA SimAnalyze. The exact antenna setup for C34-1, C34-5 and two ACA observations are input into SimObserve to recreate the exact beam used in the observation.

From the PV diagram shown in Figure 9, we found the peak location of the flat disk model has a significant offset compared to the data. The flat disk model has a peak located at  $0''.8$  position offset while the observational data have a peak located at  $0''.5$  position offset in the red-shifted side. No emission was detected in the observational data corresponding to the flat disk model’s blue-shifted peak, and this is consistent with the strong foreground absorption at  $3.1 \text{ km s}^{-1}$  fitted by total power spectrum.

We plot both the in-fall with conserved angular momentum and Keplerian rotation curves in Figure 9. In the outer region of the disk, the white Keplerian line passes through the flat Keplerian disk model and the observation data on the red-shifted side for position off-

set within  $2''.5$ . However, in the corresponding zoomed out PV diagram in Figure 4 a, for position offset greater than  $2''.5$  the white Keplerian rotation line clearly deviates from the data. Thus it is very likely the  $C^{18}O$  long tail between  $2''.5$  to  $5''.0$  corresponds to materials in-falling towards the circumbinary disk.

As discussed in section 3, we identified a blue-shifted (super-Keplerian) rotation region between  $1.5 \text{ km s}^{-1}$  and  $2.0 \text{ km s}^{-1}$  within  $1''.0$  in position offset. A clear gap between VLA1623A circumbinary disk and the blue-shifted accretion flow I can be found between  $2.3 \text{ km s}^{-1}$  to  $3.2 \text{ km s}^{-1}$  in Figure 7 as well as the PV diagram in Figure 4 a. marked by a white arrow. This gap sets a clear boundary between blue-shifted accretion flow I and the disk. This further rules out the possibility that the blue-shifted super-Keplerian rotation region is part of any large scale structures or accretion flows in the line of sight as the disk and accretion flow I are clearly separate in position and velocity space by a gap is shown in Figure 4 a. The fact that magenta in-fall velocity profile passes through the inner region of the disk, but deviates significantly on the outer edge of the circumbinary disk on the red-shift side suggests this high-velocity super-Keplerian region inside the disk has different angular momentum from the large scale accretion flows. Thus, an important question remained to be answered is whether or not the high-velocity blue-shifted component (super-Keplerian rotation region) is part of the disk structure? Is it really in-fall within the disk?



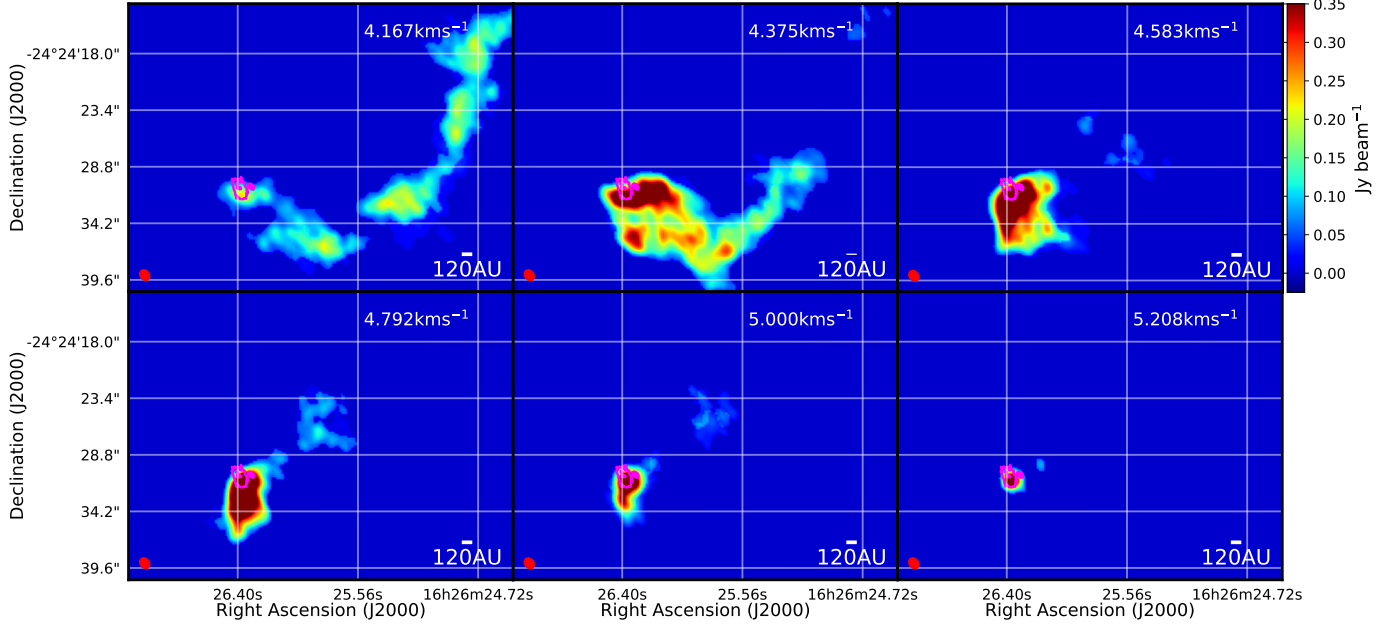


**Figure 8.** VLA1623A and red-shifted accretion flow VI channel maps. The color represents the  $C^{18}O$   $J = 2-1$  emission identified by the dendrogram algorithm. The dendrogram corresponds to the Red component (accretion flows and disk) in Cheong et al. (in prep.)’s paper. The white contours are 0.88 mm continuum data. The contours are in steps of  $5\sigma$ ,  $40\sigma$ , where  $\sigma = 5 \times 10^{-4}$   $\text{Jy beam}^{-1}$ .

In Figure 9 a the flat disk model predicts the disk with a lower position offset at high-velocity region compared to the data. This is because higher velocity traces the inner part of the Keplerian disk. Thus the inner super-Keplerian rotation region cannot be fitted by the flat disk model. For gas accreting towards the central binary, the rotation profile should be sub-Keplerian. Super-Keplerian rotation at least somewhat conserved angular momentum would result in a centrifugal force larger than the gravity, and therefore expansion.

#### 4.4. Flared Disk Model and the constraint of VLA1623 circumbinary disk’s vertical scale height

One possible explanation for this super-Keplerian rotation region is disk flaring. For a flared disk, due to the z-direction projection effect it is possible the inner region of the disk is projected to further away from the disk center. To take into account of disk flaring and projection effects, we developed a more sophisticated 3D flared disk model to model the observation data. By comparing the model with the ALMA data, we aim to constrain the density profile and the physical structure of the circumbinary disk around VLA1623A, and explain the super-Keplerian rotating region in the PV diagram.

We followed the equations of Guilloteau & Dutrey to develop a 3D flared disk model (Guilloteau, & Dutrey 1998; Yen et al. 2014). The density, velocity and tem-

perature profile are given as the following:

$$v(R) = \sqrt{\frac{GM_*}{R}} \quad (4)$$

$$T(R) = T_0 \times \left(\frac{R}{100\text{AU}}\right)^{-q} \quad (5)$$

$$\rho(R) = \rho_0 \times \left(\frac{R}{100\text{AU}}\right)^{-a} \times \exp\left(-\frac{z^2}{2h(R)^2}\right) \quad (6)$$

And the scale height relationship is given as:

$$h(R) = h_0 \times \left(\frac{R}{100\text{AU}}\right)^b \quad (7)$$

$h_0$  is the scale height of the circumbinary disk at 100 AU, and  $b$  is the flaring index. Assuming hydrostatic equilibrium, the scale height  $b = 1 + v - q/2$  with  $v = 0.5$ ,  $q = 0.4$  for a theoretical flared Keplerian disk (Guilloteau et al. 2011). The value of  $b$  is set to 1.29, using the theoretical model of flared disk (Chiang, & Goldreich 1997). The value of  $a$  follows the  $a = p + 1 + v - q/2 = 1.3 + p$ , with  $p$  being the power law index of surface density  $\Sigma = \Sigma_0 r^{-p}$  (Guilloteau, & Dutrey 1998). Considering the typical range for surface density power law  $1 \leq p \leq 2$  we explore the density power law index  $a$  in the range between 2.0 ~ 4.0.

We developed a flared disk model to constrain the density structure and vertical scale height of VLA1623A circumbinary disk. In our simple flared disk model we set

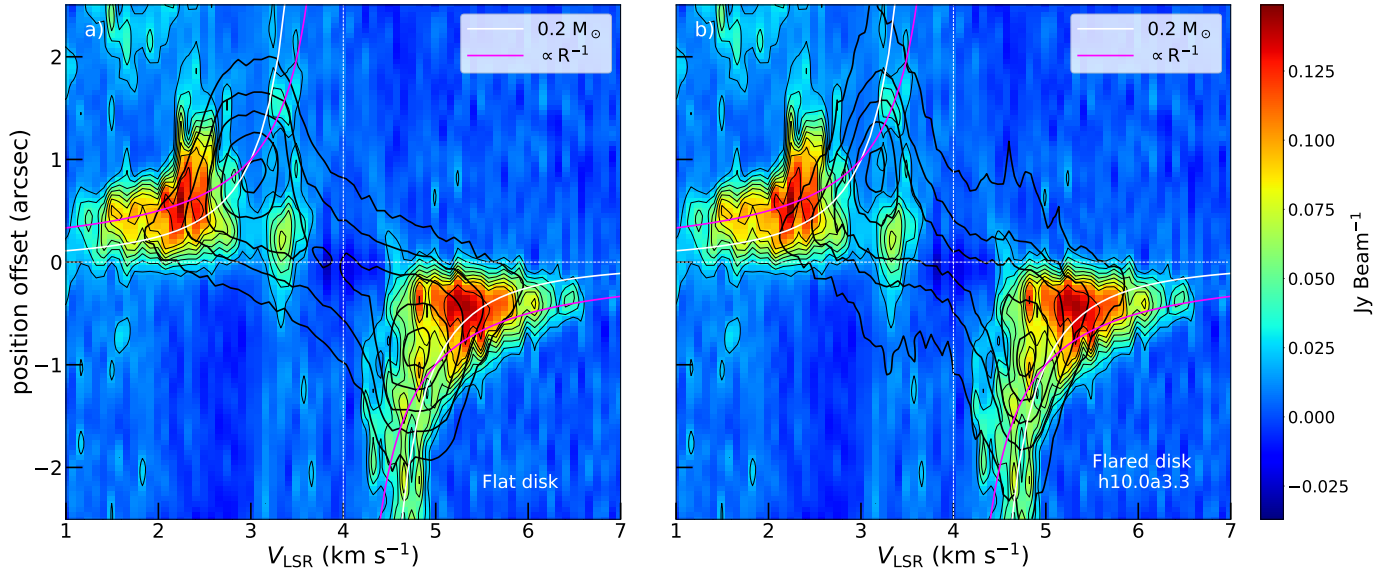


**Figure 9.** (a). Position-Velocity (PV) diagram of VLA1623A Keplerian disk and the **Flat disk model**. The color represents the PV diagram of  $C^{18}O$   $J = 2-1$  emission centered at VLA1623A. The thick black contours outline the Flat Keplerian disk model in steps of  $5\sigma$ ,  $10\sigma$ ,  $20\sigma$ ,  $30\sigma$ ,  $40\sigma$ ,  $45\sigma$ ,  $50\sigma$ , where  $\sigma = 6$  mJy beam $^{-1}$ . (b). Position-Velocity (PV) diagram of VLA1623A Keplerian disk and the **best fit Flared disk model** with vertical scale height  $h_0 = 10.0$  and power law index  $a = 3.3$ . The thick black contours outline the Flared Keplerian disk model in steps of 0.2, 0.4, 0.6, 0.8, 0.95 of the maximum flux in the model. In both panels, the white line and the magenta line represent the Keplerian rotation curve with central star mass  $0.2 M_{\odot}$  and the in-fall velocity profile with conserved specific angular momentum respectively. The color represents the PV diagram of  $C^{18}O$   $J = 2-1$  emission centered at VLA1623A and the thin black contours are plotted for  $3\sigma$ ,  $5\sigma$ ,  $7\sigma$ ,  $9\sigma$ ,  $11\sigma$ ,  $13\sigma$ ,  $15\sigma$  with  $\sigma = 9$  mJybeam $^{-1}$ .

the  $C^{18}O$  to  $H_2$  ratio to be  $1.7 \times 10^{-7}$ . The resolution of the model is  $500 \times 500 \times 500$  with each pixel at the resolution of 0.72 AU. For the density profile, we normalized the  $\rho_0$  such that the total mass of the circumbinary disk is  $0.02 M_{\odot}$  (Cheong et al. in prep.). The disk size is set to be 180 AU in radius as constrained from the  $C^{18}O$  data. The inclination angle is  $55^\circ$  and the distance is at 120 pc (Loiarnard et al. 2008; Murillo et al. 2013).

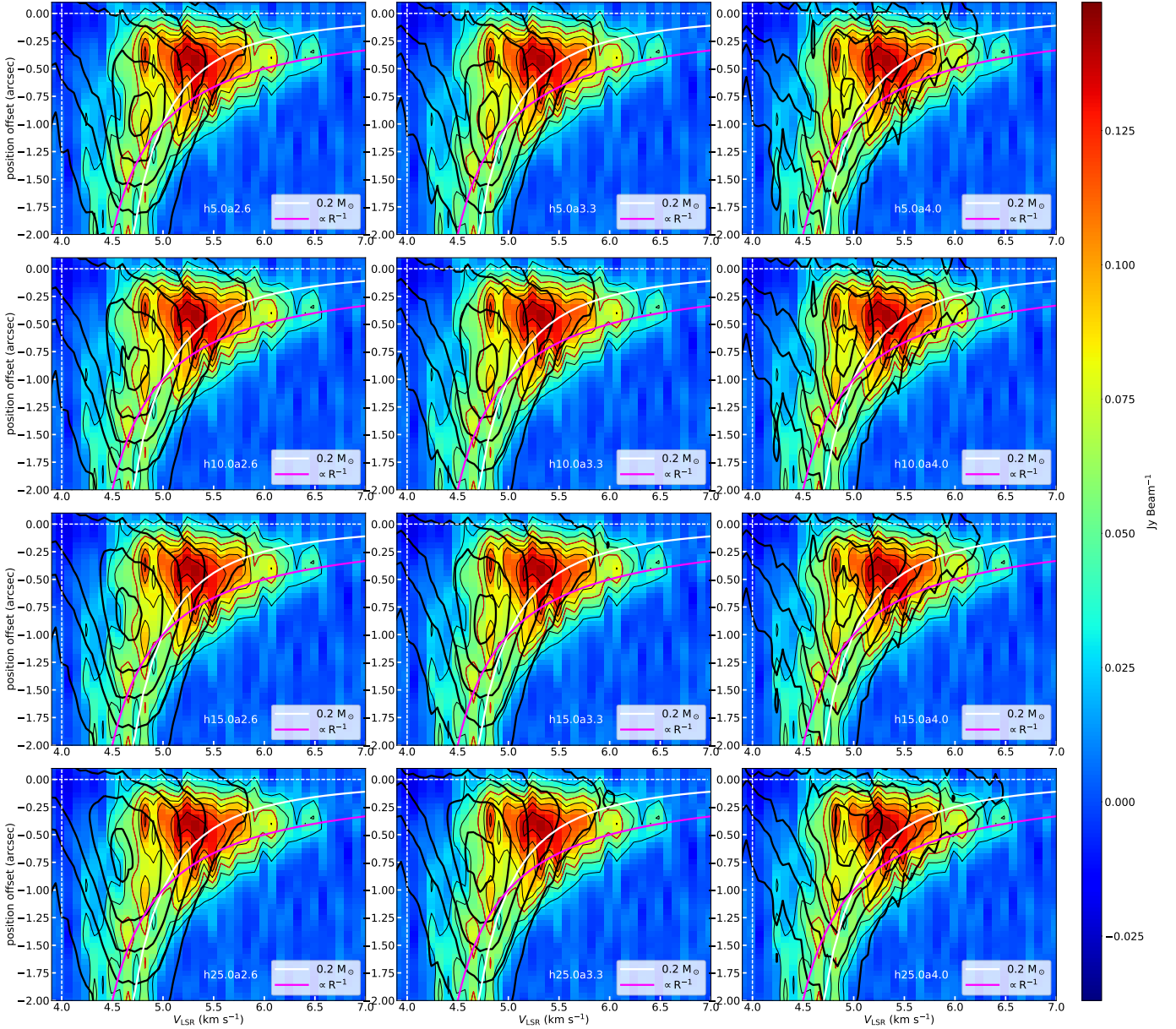
After creating the flared disk model, we use the RADMC-3D code to do radiative transfer and create synthetic images in 3D Cartesian geometries (Dullemond et al. 2012)<sup>3</sup>. The channel width output from the radiative transfer code is  $0.060$  km s $^{-1}$ . The synthetic images are then convolved with the ALMA telescope beam using CASA SimObserve and CASA SimAnalyze. Since we are interested in the density structure ( $a$ ) and the vertical structure ( $h_0$ ) of the flared circumbinary disk, we fixed the temperature  $T_0$  to be 30K at 100AU based on the DCO $^+$  data (Murillo et al. 2018).

Figure 10 display various flared disk models with different density power law index  $a$  and the vertical scale height parameter  $h_0$  for the red-shifted side of the disk. As shown in Figure 18 all the flared disk models (thick

black contours) can't explain the blue-shifted super-Keplerian rotation region in  $0''.5$  position offset at velocity range  $1.5 \sim 2.0$  km s $^{-1}$ . The mismatch between the flared disk model and the data shows that the super-Keplerian rotation region is not due to projection effects of a flared disk. If the super-Keplerian region is due to projection effects, one would expect the disk to be very flared, so the higher velocity materials in the inner region can be projected at larger position offsets. In Figure 9 the white Keplerian rotation line at  $1.5$  km s $^{-1}$  locates at position offset of  $0''.2$  ( $\sim 24$  AU) while the data locates at  $0''.5 \sim 0''.7$  ( $60 \sim 80$  AU), considering an inclination of  $55^\circ$ , if the super-Keplerian rotation region is due to project effects, then one would expect the majority of the  $C^{18}O$  is distributed around  $40 \sim 70$  AU above the disk plane. To achieve this, the scale height of the disk, location where density drops to a fraction of  $1/e$  from the mid-plane, must be much greater than 40 AU. As shown later, our flared disk models constrained the disk scale height to be within 15 AU, thus shows this super-Keplerian rotation region is not due to projection effects from a flared disk.

Comparing the models in Figure 10 and Figure 18 with observation data is very challenging. The total power spectrum reveals a huge foreground at velocity  $4.0$  km s $^{-1}$  and many small foreground absorptions on the

<sup>3</sup> RADMC-3D website: <http://www.ita.uni-heidelberg.de/~dullemond/software/radmc-3d/>



**Figure 10.** Position-Velocity (PV) diagram of VLA1623A Keplerian disk and Flared disk model with different vertical scale height  $h_0$  and density power law  $a$ . The color represents the PV diagram of  $\text{C}^{18}\text{O}$   $J = 2-1$  emission centered at VLA1623A and the thin black contours are plotted for  $3\sigma$ ,  $5\sigma$ ,  $9\sigma$ ,  $11\sigma$ ,  $13\sigma$ ,  $15\sigma$  with  $\sigma = 9 \text{ mJy beam}^{-1}$ . The brown contour marks the  $7\sigma$  line used for model comparison. The thick black contours are from the Flared Keplerian disk model. The contours are in steps of 0.2, 0.4, 0.6, 0.8, 0.95 of the maximum flux in the model. The white line represents the Keplerian rotation curve with central star mass  $0.2 M_\odot$ . The magenta line represents the in-fall velocity profile with conserved angular momentum.

blue-shifted side. Therefore, in order to eliminate the foreground effects, we only model the red-shifted part on the right side of the line corresponding to system velocity  $4.0 \text{ km s}^{-1}$ . To avoid the contamination from the outer accretion flows, we only compare the data and model within the disk radius ( $\leq 1''.5$ ).

Isophote contours for each simulation model are plotted in order to compare the observational data with simulation models. Overall we run the param-

eters  $h_0 = 1.0, 2.5, 5.0, 10.0, 15.0, 25.0$  (AU) and  $a = 2.0, 2.3, 2.6, 3.0, 3.3, 4.0$  for a total of 36 parameter combinations to examine how the central peak location changes when the scale height  $h_0$  and the density power law index  $a$  are varied.

In Figure 10 as the vertical scale height  $h_0$  increases, the model's peak (thick black contours) would shift towards the connecting bridge between blue-shifted and red-shifted region (system velocity  $4 \text{ km s}^{-1}$ , and offsets

0.0). As for the density power law index  $a$ , when  $a$  increases the PV diagram would be stretched in the direction of the Keplerian rotation line (white line). This is because when  $a$  increases, the extended part of the disk would be suppressed and the intensity peak would move closer to the disk center.

At first sight, the best fit model would be the one with density power law index  $a = 4.0$ , and scale height  $h_0 = 25.0$ . The density power law index  $a = 4.0$  suggests the peak is very compact in the center of the circumbinary disk VLA1623A. In the very high velocity region  $v > 6.0 \text{ km s}^{-1}$  and  $v < 2.0 \text{ km s}^{-1}$ , the observation data deviates from the flared disk model. The observational data doesn't follow the white Keplerian rotation line like the flared disk model, and it follows the magenta in-fall profile. This deviation suggests that an inner compact structure exists inside the VLA1623A circumbinary disk.

Thus the peak location in the observational data reflects the inner structures inside the VLA1623A circumbinary disk, not the flaring or density features of the circumbinary disk. The inner structures of VLA1623A are constrained within  $0''.5$  (60 AU) in position offset. Therefore, by modeling the data outside the  $0''.5$  (60 AU) from the inner region of the Keplerian disk, we can avoid the contamination from the inner super-Keplerian region and constrain the circumbinary disk properties. The inner structures correspond roughly to the dust ‘‘hole or gap’’ in the continuum map where the two binary components of VLA1623A are located. It is interesting that there is C18O emission from this dust gap region and that the kinematics of the gas traced by C18O deviates significantly from pure Keplerian motions, possibly indicating the accretion of fast infalling and rotating gas across the gap onto the central protobinary. Higher resolution observations are needed to test this intriguing possibility. This is discussed more in Section 4.5 below.

For the model with parameters  $a = 4.0$ ,  $h_0 = 25.0$ , we found the peak of the flared disk model has the same position offset ( $\sim 0''.5$ ) as the observation data but at a much lower velocity. In the observational data, the peak locates at the position offset  $0''.5$  and have velocity  $5.2 \text{ km s}^{-1}$ . The peak of the flared disk model and observational data does not overlap suggests that the circumbinary disk does not have density power law index  $a$  as large as 4.0. Instead, it has a relatively flatter density power law plus a compact inner structure within 60 AU from the disk center.

For density power law index  $a$  less than 3.3, there are only minor differences when  $a$  varies. The PV diagram overall is insensitive to parameter  $a$ . To prevent contamination of foreground absorption and internal structures,

we search for disk models with parameter  $a \leq 3.3$ , peak locations between  $0''.5 \sim 1''.5$  in position offset, and have emission between  $4.5 \sim 4.9 \text{ km s}^{-1}$ .

Close inspection of the fitting reveals that when the vertical scale height  $h_0$  equals to 25.0 AU, the models have peaks locate at velocity  $4.5 \sim 4.7 \text{ km s}^{-1}$  on the red-shifted side. Most importantly, in all the  $h_0 = 25.0$  models more than half of the peak area falls outside the  $7\sigma$  (63 mJy brown line in Figure 10) line on the red-shifted side. This significant offset shows that the  $h_0 = 25.0$  does not fit the data. For vertical scale height  $h_0$  less than 15 AU, the difference between the models are not significant. **Therefore, we can only constrain the density power-law  $a$  for the VLA1623A circumbinary disk to be  $a \leq 3.3$  with the vertical scale height at 100 AU to be  $h_0 \leq 15$  AU.**

It is important to highlight again that for all of the parameter sets, no model can perfectly fit the location of the peak in the PV diagram. Both flat and flared disk model does not produce peaks at the same location as the observational data. Changing vertical scale height can't produce high-velocity peaks in the inner region of the Keplerian disk, and adjusting density power law only stretches the contours along the Keplerian rotational line. Furthermore, the super-Keplerian rotation region appears on both the blue-shifted region and red-shifted region. A simple flared disk model cannot reproduce these regions indicating that the super-Keplerian rotation regions are not due to projection effects of a flared Keplerian disk. From all of the above analysis, we concluded that the high-velocity peaks in the observational data can't be explained by the structure of a rotating Keplerian disk, it must come from internal structures. In the following section, we will discuss the possibility for the binary motion of VLA1623A to produce the high-velocity peaks inside the circumbinary disk.

#### 4.5. Accretion shocks and hints for the circumprimary-circumbinary disk interactions

The flat and flared Keplerian disk modeling cannot explain the high-velocity super-Keplerian rotation region in the inner part of the disk. Previous dendrogram analysis found out a gap between accretion flows and circumbinary disk suggesting that this super-Keplerian rotation region is not coming from large scale accretion flows in the line of sight. It is within the 180 AU of the circumbinary disk. There are two possible explanations to this super-Keplerian rotation region: (i) It is coming from circumbinary-circumprimary disk interactions. (ii) The materials from above the circumbinary disk plane fall onto the inner region of the circumbinary disk. The

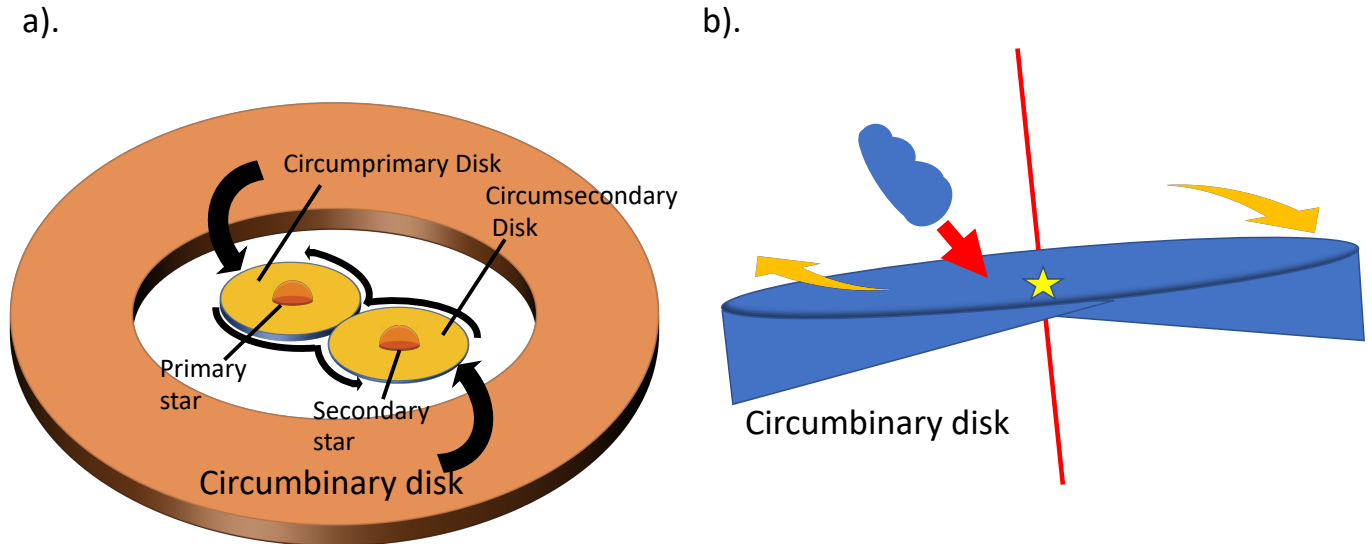


**Figure 11.** Cartoon diagram of the possible explanation of super-Keplerian rotation region in the inner region of the circumbinary disk. (a). Circumbinary-circumprimary disk interactions. (b). The materials from above the circumbinary disk plane fall onto the inner region of the circumbinary disk resulting in the net gain of angular momentum in the inner region of the disk.

collision resulted in the net gain of angular momentum in the inner region of the disk (Shown in Figure 11).

Inside the circumbinary disk, numerical simulations predict there would be smaller circumstellar (circumprimary/circumsecondary) disks around each protostar (Bate, & Bonnell 1997). Circumprimary/circumsecondary disks around binaries have typical size around  $0.35 \sim 0.5$  binary separation (Artymowicz, & Lubow 1994). The gas in circumprimary/circumsecondary disks in the binary system would experience periodic gravitational perturbation at the location of Lindblad resonance, resulting in an eccentric disk (Lubow 1991). Circumprimary/circumsecondary disks around binaries have previously been discovered in many Class I and Class II sources (GG Tau A: Dutrey et al. (2014); SR24: Mayama et al. (2010); L1551 NE: Takakuwa et al. (2017)).

VLA1623A circumbinary disk’s high-velocity blue-shifted components in the inner of the disk might be due to circumbinary-circumprimary disk interactions. The inner circumprimary/ circumsecondary disks are expected to interact with the outer circumbinary disk. Spiral accretion flows are expected to be found connecting the circumbinary and inner small disks. 2 Lagrangian points are expected to form at the connecting points of a circumbinary disk and circumprimary/ circumsecondary disks (Mayama et al. 2010). Due to the interactions between outer and inner disks, the inner region of the circumbinary disk is expected to deviate from the Keplerian rotation. Observation of rotation profile deviates from Keplerian motion in the inner region of the circumbinary disk might be a hint of the circumpri-

mary/circumbinary disk interactions. Furthermore, in Figure 1 the continuum spiral arm inside the circumbinary disk suggested the existence of small scale accretion flows within the circumbinary disk VLA1623A.

It is also possible that the apparently super-Keplerian rotation region is due to the collision between the circumbinary disk and in-falling materials from above the disk plane. Previously, we have used the dendrogram to identify large scale accretion flows. We found a 120 AU wide gap between the accretion flow I and the circumbinary disk. In order to create high-velocity  $C^{18}O$  component only in the inner region of the circumbinary disk, the in-falling materials can only collide with the circumbinary disk from above the disk plane as shown in Figure 11 b.

To determine which scenario is the case, we use SO to trace the location of shock fronts. SO with sublimation temperature of 50 K is generally attached to dust grains. Observation of SO emission indicates that it comes from collisions or shocks that give enough energy to free SO into the gas phase. Previously SO emission has been used to trace shock fronts in another similar Class 0 disk system, L1527 (Sakai et al. 2014). For the circumbinary-circumprimary disk interactions, the SO shocks will be small scale and compact located in the inner region of the circumbinary disk. For the in-fall collision’s case, the accretion flow from outside the circumbinary disk is expected to create a more extended shock front on the circumbinary disk.

Figure 12 a shows the SO  $\nu = 0, J = 8_8 - 7_7$  Moment 0 map. A strong enhancement of SO molecules near the circumbinary disk and VLA1623B is apparent

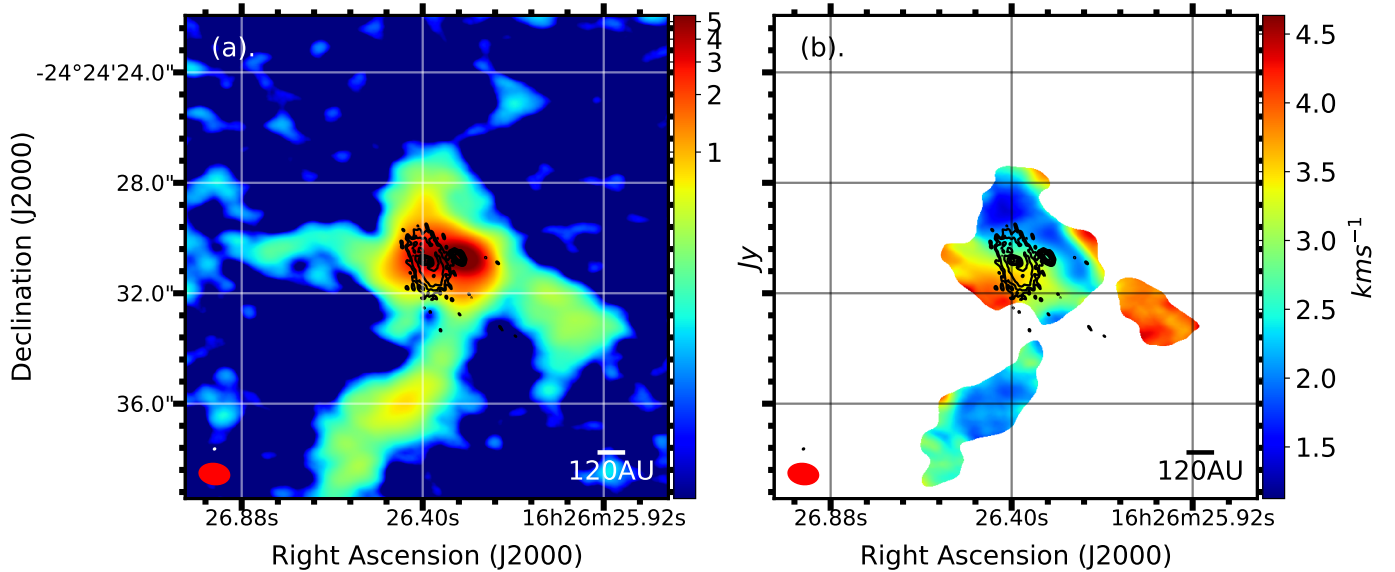


**Figure 12.** (a). SO intensity integrated map (Moment 0). The color represents the ALMA Cycle 4 SO  $\nu = 0, J = 8_8 - 7_7$  data. The black contours are 0.88 mm continuum data. The contours are in steps of  $3\sigma, 5\sigma, 10\sigma, 20\sigma, 40\sigma, 80\sigma$ , where  $\sigma = 5 \times 10^{-4} \text{ Jy beam}^{-1}$ . (b). SO mean velocity map (Moment 1).

in the moment 0 map and this indicates strong accretion shocks is created around VLA1623A circumbinary disk and VLA1623B. The SO emission shows 4 stream-like structures with two main streams to the east and south. The South stream has the strongest emission in all the streams and is connected to VLA1623B. The East stream corresponds to the red-shifted accretion flow VI identified by the dendrogram analysis using  $\text{C}^{18}\text{O}$ , and the West stream corresponds to the blue-shifted accretion flow I in Figure 6 (Red and Purple Accretion flow respectively in Cheong et al. (in prep.)).

Both the South and East stream connect to VLA1623B, and a strong emission of SO is detected on VLA1623B. The SO peaks at VLA1623B and the stream morphology suggests that on VLA1623B there exists violent shocks caused by the collision between B and the outer red-shifted accretion flow VI. As for the North and West streams, they connect to VLA1623A circumbinary disk on the map in the plane of sky. The North stream is much shorter than the South stream and this indicates the accretion flow collision is much closer toward the VLA1623A and VLA1623B from the north. In the South stream, the peak locates around  $7''$  away south from the VLA1623A binaries.

Figure 12 b shows the mean velocity map (moment 1) of SO emission around VLA1623A circumbinary disk and VLA1623B. Notice that the system velocity of VLA1623A circumbinary disk is  $4 \text{ km s}^{-1}$  and nearly all of the SO in Moment 1 map does not have a velocity greater than  $4.4 \text{ km s}^{-1}$ . The lack of red-shifted emissions in the North SO stream shows it corresponds to

the blue-shifted accretion flow I (Figure 6) flows toward the circumbinary disk. The extended high velocity SO emission in the North stream is caused by the accretion shocks due to the violent collision between the circumbinary disk and accretion flow.

As for the South SO stream, it lies in the position corresponds to the red-shifted accretion flow VI (Fig. 8). However, the accretion flow VI traced by  $\text{C}^{18}\text{O}$  is observed to be red-shifted and moving away from observer while the SO South stream is blue-shifted and moving in the opposite direction. For comparison between  $\text{C}^{18}\text{O}$  and SO data, we plot the  $\text{C}^{18}\text{O}$   $J = 2-1$  intensity integrated map (Moment 0) between  $3.29 \text{ km s}^{-1} \sim 4.43 \text{ km s}^{-1}$  in Figure 13 a and between  $1.27 \text{ km s}^{-1} \sim 2.21 \text{ km s}^{-1}$  in Figure 13 b with SO data display as black contours in both figures.

In Figure 13 a, the  $\text{C}^{18}\text{O}$  emission which corresponds to the materials at low blue-shifted velocity and at rest is much more extended than the Southern SO stream.  $\text{C}^{18}\text{O}$  at rest are mostly distributed on the south side of the circumbinary disk and VLA1623B. Materials are piled up in the south, and this wall-like structure would be discussed in the next section.

One of the most prominent features in Figure 13 b is the Northern and Southern arm. The Northern  $\text{C}^{18}\text{O}$  arm corresponds to the accretion flow III (See Figure 6). The Southern  $\text{C}^{18}\text{O}$  arm has the same velocity range as the SO south stream and it overlays in the line of sight perfectly. From the dendrogram analysis carried out by Cheong et al. (in prep.), the Southern arm corresponds to the Structure II in Figure 6. Cheong et al.

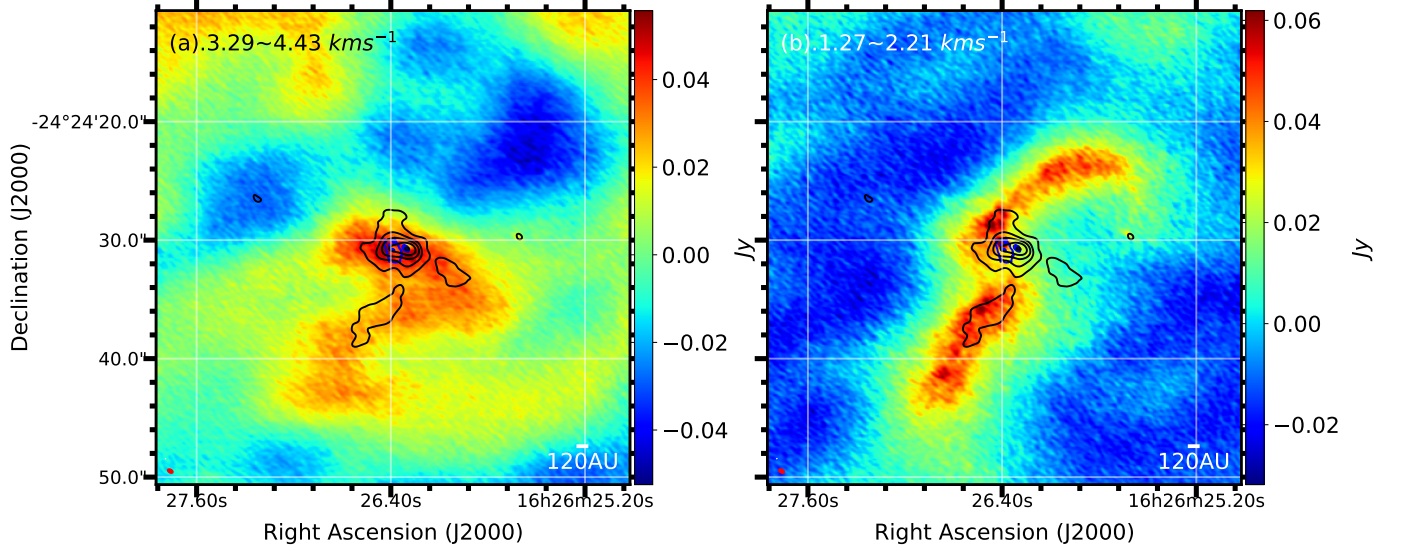


**Figure 13.** (a).  $C^{18}O$   $J = 2-1$  intensity integrated map (Moment 0) between  $3.29 \text{ km s}^{-1}$  and  $4.43 \text{ km s}^{-1}$ . (b).  $C^{18}O$   $J = 2-1$  intensity integrated map (Moment 0) between  $1.27 \text{ km s}^{-1}$  and  $2.21 \text{ km s}^{-1}$ . The color in both panels represent the  $C^{18}O$  data. The black contours are ALMA Cycle 4 SO  $\nu = 0, J = 8_8 - 7_7$  data. The contours are in steps of 0.025, 0.05, 0.1, 0.2, 0.4, 0.8 of the maximum intensity which is  $8.5 \text{ Jy beam}^{-1}$ . The central blue contours are 0.88 mm continuum data in steps of  $5\sigma$ ,  $40\sigma$ , where  $\sigma = 5 \times 10^{-4} \text{ Jy beam}^{-1}$ . The continuum data marked the position of the VLA1623A circumbinary disk and VLA1623B.

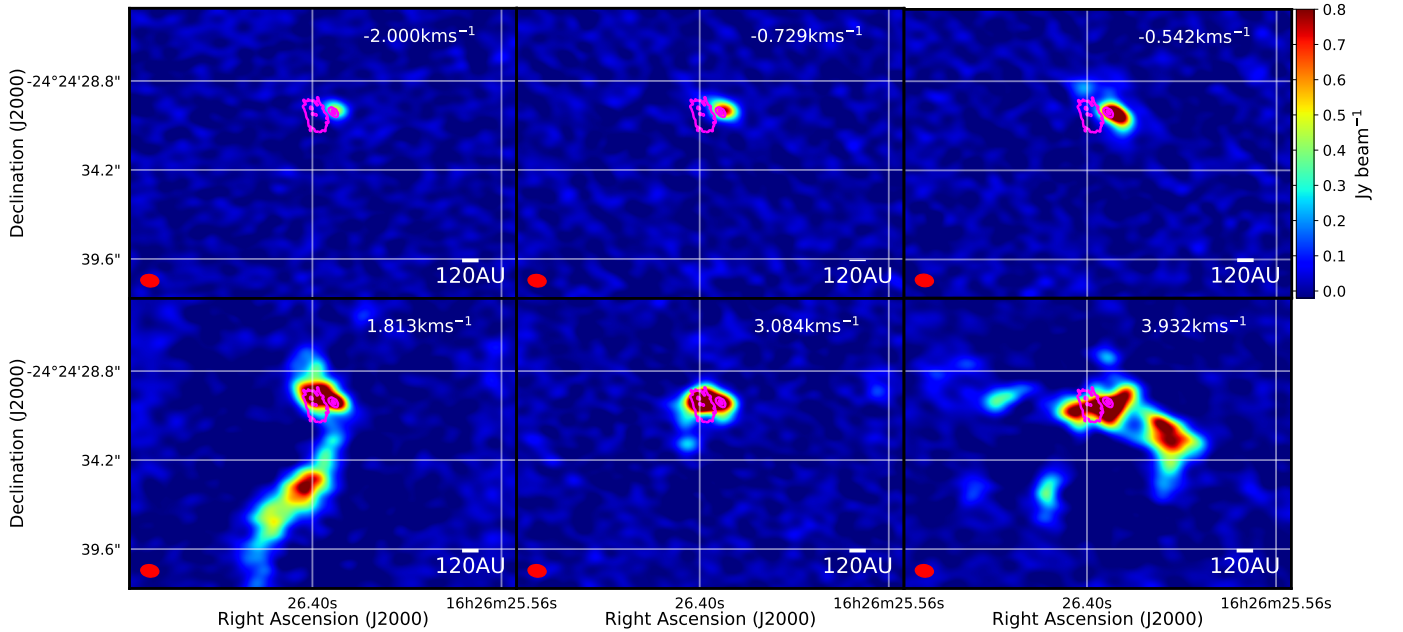


**Figure 14.** SO channel maps. The color represents the ALMA Cycle 4 SO  $\nu = 0, J = 8_8 - 7_7$  data. The black contours are 0.88 mm continuum data in steps of  $3\sigma$ ,  $5\sigma$ ,  $40\sigma$ ,  $80\sigma$ , where  $\sigma = 5 \times 10^{-4} \text{ Jy beam}^{-1}$ .

(in prep.) further carried out the CMU model analysis (Ulrich 1976; Cassen, & Moosman 1981), a rotating collapse model with conserved specific angular momentum, and found the blue-shifted component II does not match the CMU model. This indicates the materials falling from the South stream do not follow the parabolic trajectories. From the dendrogram analysis, CMU fitting in Cheong et al. (in prep.) we concluded that the

South SO stream of (Figure 12 a & b) corresponds to the accretion flows with non-conserved specific angular momentum, possibly affected by outflows from the protostellar sources.

After identifying the corresponding SO streams around VLA1623A circumbinary disk by comparing with the  $C^{18}O$  data, PV diagrams are used to further study their interactions. We plot the PV diagrams of

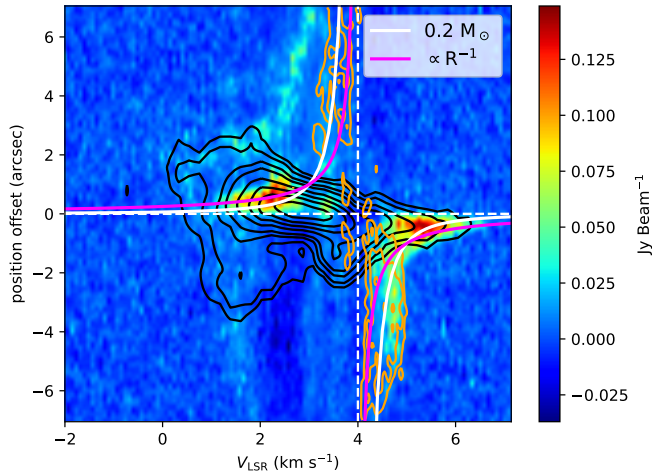


**Figure 15.** ALMA Cycle 4 SO ( $\nu = 0, J = 8_8 - 7_7$ , black contours), ALMA Cycle 2  $C^{18}O$  ( $J = 2-1$ , color), and DCO+ ( $J = 3-2$ , orange) position velocity (PV) diagram on **VLA1623A**. The contours are in steps of  $5\sigma$ ,  $10\sigma$ ,  $20\sigma$ ,  $30\sigma$ ,  $50\sigma$ ,  $70\sigma$ ,  $90\sigma$ , where  $\sigma = 15$ ,  $4.4 \text{ mJy beam}^{-1}$  for SO and DCO+ respectively. The magenta solid line is the in-fall profile with conserved angular momentum, and the white solid line is the Keplerian rotation profile with central stellar mass of  $0.2 M_{\odot}$ .

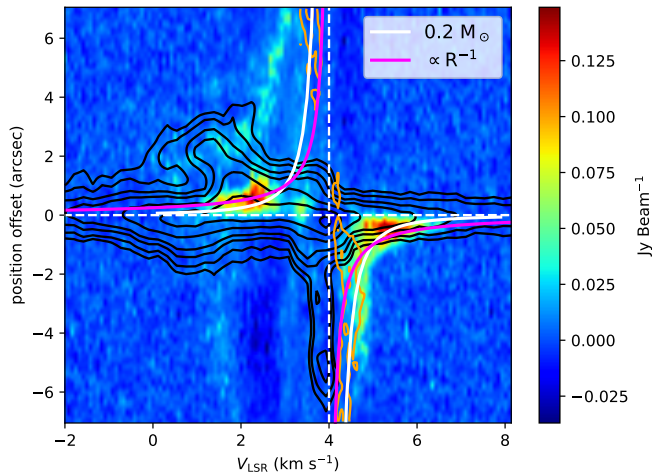


**Figure 16.** ALMA Cycle 4 SO ( $\nu = 0, J = 8_8 - 7_7$ , black contours), ALMA Cycle 2  $C^{18}O$  ( $J = 2-1$ , color), and DCO+ ( $J = 3-2$ , orange) position velocity (PV) diagram on **VLA1623B**. The contours are in steps of  $5\sigma$ ,  $10\sigma$ ,  $20\sigma$ ,  $30\sigma$ ,  $50\sigma$ ,  $70\sigma$ ,  $90\sigma$ , where  $\sigma = 15$ ,  $8 \text{ mJy beam}^{-1}$  for SO and DCO+ respectively. The magenta solid line is the in-fall profile with conserved angular momentum, and white solid line is the Keplerian rotation profile with central stellar mass of  $0.2 M_{\odot}$ . Note that the central velocity of SO is shifted to  $3 \text{ km s}^{-1}$ .

SO ( $J = 8_8 - 7_7$ ),  $C^{18}O$  ( $J = 2-1$ ), and DCO+ ( $J = 3-2$ ) across VLA1623A circumbinary disk in Figure 15. The PV cut is cut along the red line shown in Figure 2. The black SO contours marked out the extended high veloc-

ity SO emission on the blue-shifted side. It spreads out from  $-4''0 \sim 2''0$  with the center of the circumbinary disk positioned at  $0''0$ . The spatially extended high velocity SO on the blue-shifted side suggests there are violent accretion shocks, which are likely produced by the interaction between the accretion flow I and the circumbinary disk, although a contribution from interaction with an outflow cannot be ruled out at this time. In contrast, the SO on the red-shifted part is very spatially compact and locates only in the center of the circumbinary disk. The compact structure of the red-shifted SO suggests that there is no violent accretion shocks between the red-shifted accretion flow VI and the circumbinary disk around VLA1623A.

To sum up, we use SO as a shock tracer to identify possible accretion shocks between the circumbinary disk and the blue-shifted accretion flow I. The SO data have beam size around  $1''1$ , and thus the large size of the beam will smear out all the compact SO components due to circumprimary-circumbinary disk interactions. Higher resolution data is needed to confirm whether or not the central gas motion is due to circumprimary-circumbinary disk interactions (in-fall in the disk plane) or collision from in-falling gas above the disk plane. Even with the limited resolution, the **SO data shows no sign of accretion shocks on the red-shifted part of the VLA1623A circumbinary disk (Figure 15)**. On the red-shifted part, the observation of inner super-Keplerian rotation region in Figure 9 gives strong evidence supporting the existence of inner structures of VLA1623A circumbinary disk.

Furthermore, **the inner super-Keplerian rotation region in Figure 9 follows the in-fall with conserved angular momentum velocity profile.  $C^{18}O$  gas free fall towards the central binaries indicates the existence of inner cavity around the VLA1623A binaries (Figure 11 a.)**. The central binary has cleared out the surrounding gas separating them from the large Keplerian rotating circumbinary disk. The materials can only transfer from the circumbinary disk to the central binaries via in-fall with conserved angular momentum.

#### 4.6. Existence of Wall-like structure south of VLA1623B

The PV diagrams of SO ( $J = 8_8 - 7_7$ ),  $C^{18}O$  ( $J = 2-1$ ), and DCO+ ( $J = 3-2$ ) on VLA1623B, centered at  $\alpha(J2000) = 16^{\text{h}}26^{\text{m}}26^{\text{s}}.305$ ,  $\delta(J2000) = -24^{\circ}24'30''.705$  with position angle of  $222.8^{\circ}$  are plotted in Figure 16. In the blue-shifted region at the position offset around  $3''0$ , we observed the similar extended high velocity blue-shifted SO feature compare to Figure 15, which corre-



sponds to the shock fronts of the accretion flow I. The SO emission has a very wide line width ( $>10 \text{ km s}^{-1}$ ) at the position offset between  $\pm 1''0$  (across VLA1623B). The huge velocity dispersion on VLA1623B indicates there is a huge change in velocity on VLA1623B and huge shock fronts are formed. Furthermore, at the south of VLA1623B the materials only have velocity around  $4.0 \text{ km s}^{-1}$  suggesting the SO is at rest. The huge change in SO velocity and materials ( $\text{C}^{18}\text{O}$ , SO,  $\text{DCO}^+$ ) on the south of the VLA1623B are at rest both suggests a wall-like structure is located south of VLA1623B.

In the previous section, the red-shifted accretion flow VI is identified to be connecting to VLA1623B (See Figure 6, Figure 8). When the materials from the blue-shifted accretion flow III accrete onto VLA1623B, they are quickly stopped by the red-shifted accretion flow VI (shown in Figure 8). The collision between blue-shifted accretion flow III and red-shifted accretion flow VI on VLA1623B slows down the materials and forms an extended wall-like structure south of VLA1623B. This explains why no violent accretion shocks from the red-shifted accretion flow VI is observed around VLA1623A circumbinary disk. The red-shifted accretion flow VI is already significantly slowed down around VLA1623B.

To constrain the size of the wall-like structure south of VLA1623B, we analyze the SO PV diagram in Figure 16. In Figure 16, around the systematic velocity  $4 \text{ km s}^{-1}$  there exists a long extended SO and  $\text{DCO}^+$  on the south (negative offset) side of VLA1623B.  $\text{DCO}^+$  would have abundance enhancement when the temperature is below CO freeze-out temperature (Mathews et al. 2013). However,  $\text{DCO}^+$  emission at rest around the disk is contaminated from the envelope making it not ideal to trace the wall-like structure south of the circumbinary disk. On the other hand, SO which has high sublimation temperature of  $50\text{K}$  traces the shocks region near the centrifugal barrier (Sakai et al. 2014). The SO in Figure 16 extends to around  $6''.5$  ( $\sim 780 \text{ AU}$ ). Therefore, the wall on the south side of VLA1623B has a plane of sky width at least  $780 \text{ AU}$ .

## 5. DISCUSSIONS

The results of flat and flared disk modeling show that VLA1623A circumbinary disk is a large flat Keplerian disk with a size of  $180 \text{ AU}$  and a vertical scale height less than  $15 \text{ AU}$  at  $r = 100 \text{ AU}$ . At the edge of the circumbinary disk, it is calculated to have a thickness less than  $64 \text{ AU}$ . This is consistent with the result of CMU modeling, which shows the thickness of the incoming accretion flows at the centrifugal radius is around  $30 \text{ AU}$  (Cheong et al. in prep.).

**Table 3.** Accretion flows around VLA1623A

Accretion flow	Velocity ( $\text{km s}^{-1}$ )	SO data	$\text{C}^{18}\text{O}$ data
I	$2.02 \sim 3.60$	Figure 12 West SO stream	Figure 7
II	$1.27 \sim 2.21$	Figure 12 South SO stream	Figure 13 b South $\text{C}^{18}\text{O}$ stream
III	$1.27 \sim 2.21$	Figure 12 North SO stream	Figure 13 b North $\text{C}^{18}\text{O}$ stream
VI	$3.45 \sim 4.79$	Figure 12 East SO stream	Figure 8, 13 a East $\text{C}^{18}\text{O}$ clump

In the previous sections, we used both SO  $J = 8_s - 7_7$  and  $\text{C}^{18}\text{O}$   $J = 2-1$  data to study how the accretion flows interact with the circumbinary disk around VLA1623A and VLA1623B. A cartoon diagram of their interactions is summarized in Figure 17. In short, there are around 4 main accretion flows found in this study: blue-shifted accretion flow I, II, III, and red-shifted accretion flow VI as summarized in Table 3.

From the extended emission in the SO PV diagram (Figure 15), we identified an accretion shock north of the circumbinary disk around VLA1623A. This SO accretion shocks are produced by the blue-shifted accretion flows I and III colliding with the edge of the circumbinary disk. The blue-shifted accretion flow III also collide with the red-shifted accretion flows VI on VLA1623B (Figure 16). The collision creates extremely wide SO line width ( $> 10 \text{ km s}^{-1}$ ) corresponding to the violent shocks on VLA1623B. The collision significantly slows down and stop the materials from the red-shifted accretion flows VI at a position south of the VLA1623B forming a wall-like structure as shown in Figure 16.

The materials from red-shifted accretion flow VI continue to pile up, spread to the south of VLA1623A circumbinary disk and in-fall towards it. The in-fall rotating materials are connected to the boundary of the disk and extended up to  $\sim 500 \text{ AU}$  south of the circumbinary disk. This explains the extended red-shifted  $\text{C}^{18}\text{O}$  emission in Figure 3. Furthermore, the blue-shifted accretion flow II collides with this in-fall rotating materials and forms a long extended SO South stream in Figure 12 with a peak located around  $4''0$  south from the disk. The overall picture of the interactions between accretion flows and circumbinary disk around VLA1623A and VLA1623B is summarized in Figure 17.

## 6. CONCLUSIONS

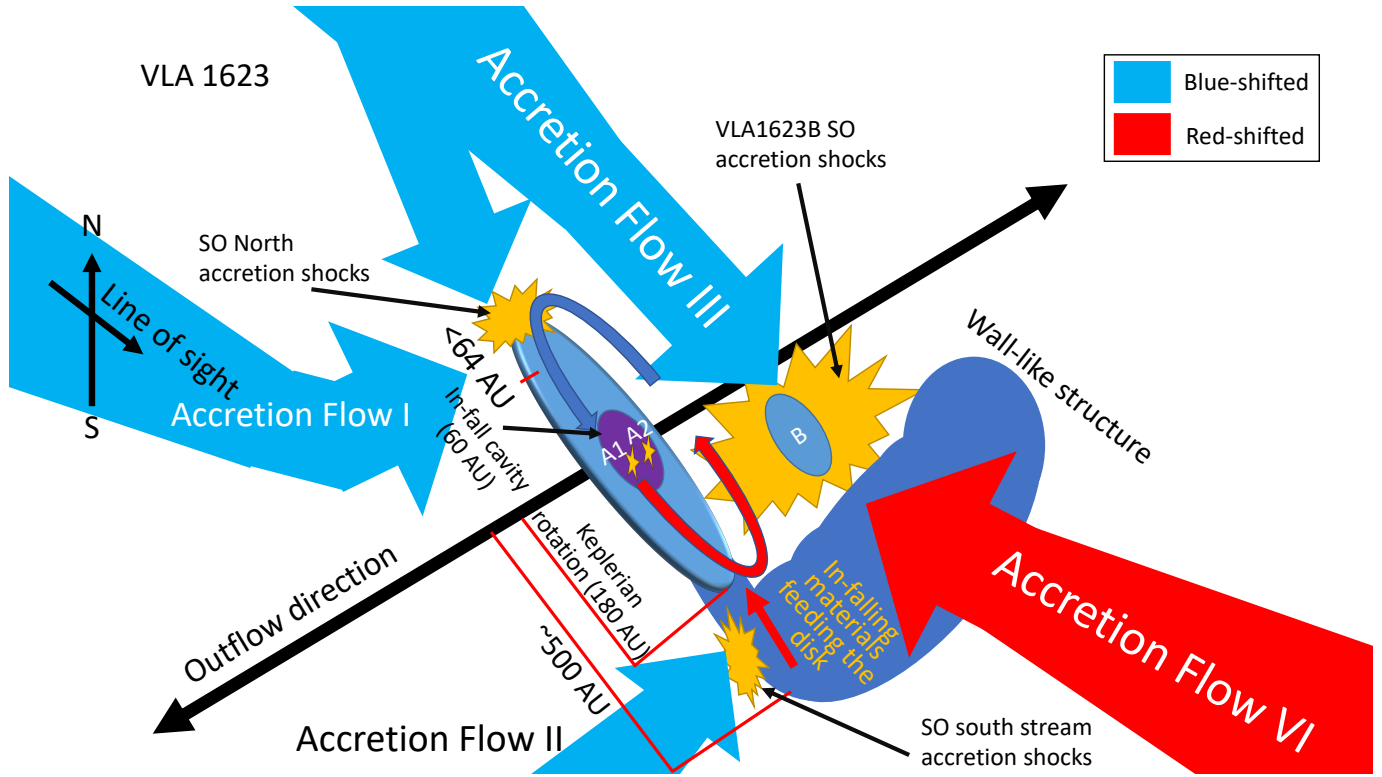


**Figure 17.** Cartoon diagram of accretion flows and disk interactions studied in this work towards VLA1623A circumbinary disk and VLA1623B.

This work presents a detailed analysis of VLA1623A circumbinary disk and VLA1623B. The results can be summarized as the following:

1. By comparing the data with flared disk models, we found the circumbinary disk around VLA1623A has a vertical scale height less than 15 AU at a radius of 100 AU. The circumbinary disk around VLA1623A is found to be very large and flat.
2. From the SO PV diagrams, we detect the existence of a wall-like structure south of VLA1623B. The wall has a plane of sky width of around 780 AU on the VLA1623B side. Furthermore, a plausible picture of how accretion flows interact with VLA1623A circumbinary disk and VLA1623B is constructed and shown in Figure 17.
3. The super-Keplerian rotation region inside the VLA1623A circumbinary disk cannot be fitted properly with either Flat or Flared Keplerian disk models. We suggest this emission traces infalling streamers that feed material from the circumbinary disk onto the central VLA1623A binaries. This in-fall with conserved angular momentum velocity profile (Figure 4) is direct evidence showing that the central binary opens up a cavity inside the

circumbinary disk around VLA1623A, and the gas traced by  $C^{18}O$  can cross this cavity to feed the central binary.

CHH and SPL acknowledge support from the Ministry of Science and Technology of Taiwan with Grant MOST 106-2119-M-007-021-MY3. ZYL is supported in part by NASA grant 80NSSC18K1095 and NNX14B38G and NSF grant AST-1815784 and 1716259. The authors further thank Héctor Arce and Paolo Coppi for helpful discussions and/or for commenting on drafts of this manuscript. This paper makes use of the following ALMA data: ADS/JAO.ALMA #2011.0.00902.S, #2013.1.01004S, #2015.1.00084S, #2016.1.01468. ALMA is a partnership of ESO (representing its member states), NSF (USA) and NINS (Japan), together with NRC (Canada) and NSC and ASIAA (Taiwan) and KASI (Republic of Korea), in cooperation with the Republic of Chile. The Joint ALMA Observatory is operated by ESO, AUI/NRAO and NAOJ. The National Radio Astronomy Observatory is a facility of the National Science Foundation operated under cooperative agreement by Associated Universities, Inc.

## REFERENCES

- Andre, P., Martin-Pintado, J., Despois, D., et al. 1990, *A&A*, 236, 180.
- Artymowicz, P., & Lubow, S. H. 1994, *ApJ*, 421, 651.
- Andre, P., Ward-Thompson, D., & Barsony, M. 1993, *ApJ*, 406, 122.
- Aso, Y., Ohashi, N., Aikawa, Y., et al. 2017, *ApJ*, 849, 56
- Bate, M. R., & Bonnell, I. A. 1997, *MNRAS*, 285, 33.
- Beaumont, C., Robitaille, T., & Borkin, M. 2014, *Glue: Linked data visualizations across multiple files*, ascl:1402.002.
- Boss, A. P., & Keiser, S. A. 2014, *ApJ*, 794, 44.
- Burkert, A., & Bodenheimer, P. 1993, *MNRAS*, 264, 798.
- Cassen, P., & Moosman, A. 1981, *Icarus*, 48, 353.
- Chiang, E. I., & Goldreich, P. 1997, *ApJ*, 490, 368.
- Chou, T.-L., Takakuwa, S., Yen, H.-W., et al. 2014, *ApJ*, 796, 70.
- Connelley, M. S., Reipurth, B., & Tokunaga, A. T. 2008, *AJ*, 135, 2526.
- Lee, C.-F., Li, Z.-Y., Ho, P. T. P., et al. 2017, *ApJ*, 843, 27.
- Davidson, J. A., Novak, G., Matthews, T. G., et al. 2011, *ApJ*, 732, 97.
- Dent, W. R. F., Matthews, H. E., & Walther, D. M. 1995, *MNRAS*, 277, 193.
- Duchêne, G., Bontemps, S., Bouvier, J., et al. 2007, *A&A*, 476, 229.
- Dullemond, C. P., Juhasz, A., Pohl, A., et al. 2012, *Astrophysics Source Code Library*, ascl:1202.015.
- Dutrey, A., di Folco, E., Guilloteau, S., et al. 2014, *Nature*, 514, 600.
- Dutrey, A., Di Folco, E., Beck, T., et al. 2016, *Astronomy and Astrophysics Review*, 24, 5.
- Fromang, S., & Stone, J. M. 2009, *A&A*, 507, 19.
- Guan, X., & Gammie, C. F. 2009, *ApJ*, 697, 1901.
- Guilloteau, S., & Dutrey, A. 1998, *A&A*, 339, 467.
- Guilloteau, S., Dutrey, A., Piétu, V., et al. 2011, *A&A*, 529, A105.
- Harris, R. J., Cox, E. G., Looney, L. W., et al. 2018, *ApJ*, 861, 91.
- Hennebelle, P., & Ciardi, A. 2009, *A&A*, 506, L29.
- Hennebelle, P., Commerçon, B., Chabrier, G., et al. 2016, *ApJ*, 830, L8.
- Hull, C. L. H., Plambeck, R. L., Bolatto, A. D., et al. 2013, *ApJ*, 768, 159.
- Hull, C. L. H., Plambeck, R. L., Kwon, W., et al. 2014, *The Astrophysical Journal Supplement Series*, 213, 13.
- Inutsuka, S.-I., & Miyama, S. M. 1992, *ApJ*, 388, 392.
- Jørgensen, J. K., van Dishoeck, E. F., Visser, R., et al. 2009, *A&A*, 507, 861.
- Lesur, G., & Longaretti, P.-Y. 2009, *A&A*, 504, 309.
- Lizano, S., Tapia, C., Boehler, Y., et al. 2016, *ApJ*, 817, 35.
- Loinard, L., Torres, R. M., Mioduszewski, A. J., et al. 2008, *ApJ*, 675, L29.
- Lubow, S. H. 1991, *ApJ*, 381, 259.
- Mathews, G. S., Klaassen, P. D., Juhász, A., et al. 2013, *A&A*, 557, A132.
- Mayama, S., Tamura, M., Hanawa, T., et al. 2010, *Science*, 327, 306.
- Mellon, R. R., & Li, Z.-Y. 2008, *ApJ*, 681, 1356.
- Murillo, N. M., Lai, S.-P., Bruderer, S., et al. 2013, *A&A*, 560, A103.
- Murillo, N. M., & Lai, S.-P. 2013, *ApJ*, 764, L15.
- Murillo, N. M., van Dishoeck, E. F., van der Wiel, M. H. D., et al. 2018, *ArXiv e-prints*, arXiv:1805.05205.
- Offner, S. S. R., Kratter, K. M., Matzner, C. D., et al. 2010, *ApJ*, 725, 1485.
- Ortiz-León, G. N., Loinard, L., Kounkel, M. A., et al. 2017, *ApJ*, 834, 141.
- Padoan, P., & Nordlund, Å. 2002, *ApJ*, 576, 870.
- Pineda, J. E., Offner, S. S. R., Parker, R. J., et al. 2015, *Nature*, 518, 213.
- Raghavan, D., McAlister, H. A., Henry, T. J., et al. 2010, *The Astrophysical Journal Supplement Series*, 190, 1.
- Sakai, N., Sakai, T., Hirota, T., et al. 2014, *Nature*, 507, 78.
- Santangelo, G., Murillo, N. M., Nisini, B., et al. 2015, *A&A*, 581, A91.
- Sana, H., & Evans, C. J. 2011, *Active OB Stars: Structure, Evolution, Mass Loss, and Critical Limits*, 474.
- Schekochihin, A. A., Cowley, S. C., Maron, J. L., et al. 2004, *PhRvL*, 92, 54502.
- Shu, F. H., Adams, F. C., & Lizano, S. 1987, *Annual Review of Astronomy and Astrophysics*, 25, 23.
- Shu, F. H., Galli, D., Lizano, S., et al. 2007, *ApJ*, 665, 535.
- Takakuwa, S., Saito, M., Lim, J., et al. 2012, *ApJ*, 754, 52.
- Takakuwa, S., Saigo, K., Matsumoto, T., et al. 2017, *ApJ*, 837, 86.
- Tobin, J. J., Hartmann, L., Chiang, H.-F., et al. 2013, *ApJ*, 771, 48.
- Tobin, J. J., Bos, S. P., Dunham, M. M., et al. 2018, *ApJ*, 856, 164.
- Tomida, K., Okuzumi, S., & Machida, M. N. 2015, *ApJ*, 801, 117.
- Tang, Y.-W., Dutrey, A., Guilloteau, S., et al. 2014, *ApJ*, 793, 10.
- Tang, Y.-W., Dutrey, A., Guilloteau, S., et al. 2016, *ApJ*, 820, 19.
- Ulrich, R. K. 1976, *ApJ*, 210, 377.
- Yen, H.-W., Takakuwa, S., Ohashi, N., et al. 2013, *ApJ*, 772, 22.

Yen, H.-W., Takakuwa, S., Ohashi, N., et al. 2014, ApJ, 793, 1.

Yu, T., & Chernin, L. M. 1997, ApJ, 479, L63.

## APPENDIX

Figure 18 displays the results of the flared disk modeling without zoomed in on the red-shifted components.

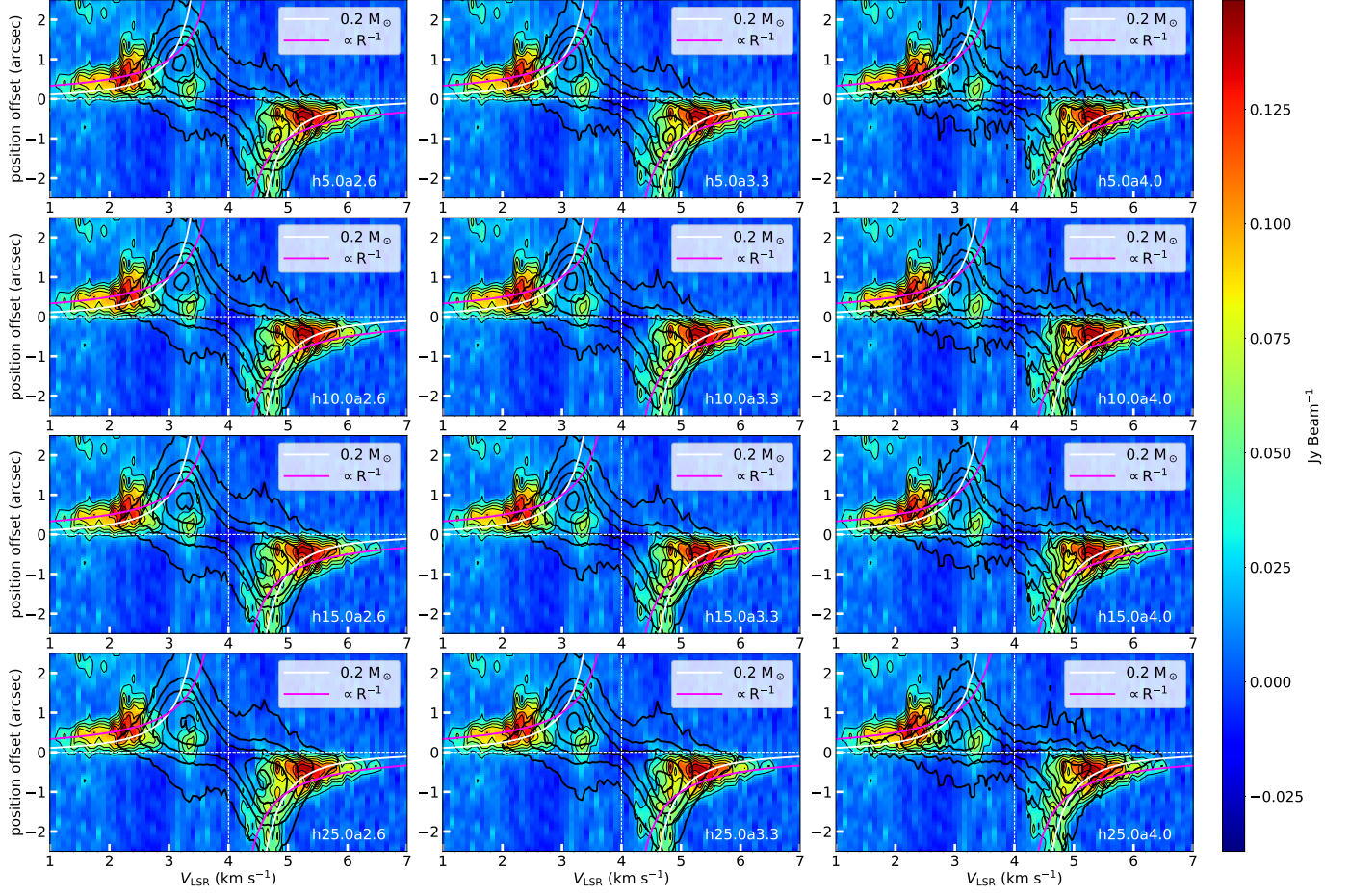


**Figure 18.** Position-Velocity (PV) diagrams of VLA1623A Keplerian disk and Flared disk model with different vertical scale height  $h_0$  and density power-law  $a$ . The color represents the PV diagram of  $\text{C}^{18}\text{O}$   $J = 2-1$  emission centered at VLA1623A and the thin black contours are plotted for  $3\sigma$ ,  $5\sigma$ ,  $7\sigma$ ,  $9\sigma$ ,  $11\sigma$ ,  $13\sigma$ ,  $15\sigma$  with  $\sigma = 9 \text{ mJy beam}^{-1}$ . The thick black contours are from the Flared Keplerian disk model. The contours are in steps of 0.2, 0.4, 0.6, 0.8, 0.95 of the maximum flux in the model. The white line represents the Keplerian rotation curve with central star mass  $0.2 M_\odot$ . The magenta line represents the in-fall velocity profile with conserved angular momentum.